

Probing nuclear interactions à la Rutherford: Insights on ^4He from α scattering

F. Cappuzzello^{1,2}, V. Soukeras^{1,2*}, S. Bacca^{3,4}, D. Carbone²,
M. Cavallaro², L. C. Chamon⁵, I. Lombardo^{1,6}, G. Orlandini^{7,8},
M. Viviani⁹, C. Agodi², H -W. Becker¹⁰, G. A. Brischetto^{1,2},
S. Calabrese², C. Ciampi¹¹, M. Cicerchia^{12,13}, M. Cinausero¹⁴,
I. Ciraldo^{1,2}, D. Dell’Aquila^{15,16}, M. Fisichella², C. Frosin¹¹,
A. Hacisalihoglu^{2,17}, M. Hilcker¹⁸, A. Kievsky⁸, Y. Kucuk^{19,20},
T. Marchi¹², O. Sgouros^{1,2}, A. Spatafora^{1,2}, D. Torresi²,
M. Vigilante^{15,16}, A. Yildirim²⁰

¹Dipartimento di Fisica e Astronomia “Ettore Majorana”, Università di Catania, Catania, Italy.

²INFN – Laboratori Nazionali del Sud (LNS), Catania, Italy.

³Institut für Kernphysik, Johannes Gutenberg-Universität Mainz, Mainz, Germany.

⁴Helmholtz-Institut Mainz, Johannes Gutenberg-Universität Mainz, Mainz, Germany.

⁵Departamento de Física Nuclear, Instituto de Física da Universidade de São Paulo, São Paulo, Brazil.

⁶INFN – Sezione di Catania, Catania, Italy.

⁷Dipartimento di Fisica, Università di Trento, Trento, Italy.

⁸INFN - Trento Institute for Fundamental Physics and Applications (TIFPA), Trento, Italy.

⁹INFN – Sezione di Pisa, Pisa, Italy.

¹⁰Ruhr-Universität Bochum, Bochum, Germany.

¹¹INFN – Sezione di Firenze, Firenze, Italy.

¹²Dipartimento di Fisica e Astronomia, Università di Padova, Padova, Italy.

¹³INFN – Sezione di Padova, Padova, Italy.

¹⁴INFN – Laboratori Nazionali di Legnaro (LNL), Legnaro, Italy.

¹⁵Dipartimento di Fisica “Ettore Pancini”, Università degli Studi di Napoli “Federico II”, Napoli, Italy.

¹⁶INFN – Sezione di Napoli, Napoli, Italy.

¹⁷Institute of Natural Science, Karadeniz Teknik Universitesi, Trabzon, Turkey.

¹⁸Department of Physics, Institute for Nuclear Physics, Technische Universität Darmstadt, Darmstadt, Germany.

¹⁹Turkish Accelerator and Radiation Laboratory (TARLA), Gölbaşı/Ankara, Türkiye.

²⁰Akdeniz University, Antalya, Turkey.

*Corresponding author(s). E-mail(s): vasileios.soukeras@lns.infn.it;

Abstract

Nuclear interactions play a key role for the stability of atomic nuclei and stellar environments. Successful parametrization and models of these interactions, developed in the last decades, accurately reproduce all the proton and neutron scattering data, besides the properties of few-body nuclear systems. However, recent electron scattering results focusing on the first excited resonant state of ${}^4\text{He}$ nucleus, reveal a puzzling situation suggesting potential gaps in our understanding of the nuclear phenomenology. Here, we report a new study of such ${}^4\text{He}$ resonance by ${}^4\text{He} + {}^4\text{He}$ scattering featuring data of unprecedented sensitivity and state-of-art analyses of the spectral line shape together with a phenomenological reaction modeling that incorporates the same nuclear densities employed in electron-scattering studies. Our analysis of the full set of experimental observables yields a reasonable description within the framework of current nuclear-interaction physics, thereby highlighting the need for further advancing the modeling of few-body open quantum systems.

1 Introduction

Ernest Rutherford’s scattering experiments with α particles, aka ${}^4\text{He}$ nuclei in their ground state, led to the groundbreaking discovery of the atomic nucleus over a century ago [1], revolutionized our understanding of atomic structure and laid the foundation for modern nuclear physics. Building on this rich legacy, in this paper we delve into the contemporary exploration of α scattering employing new technologies and methods developed since Rutherford’s time with the goal of shedding light onto an intriguing quantum mechanical problem involving the α particle itself.

The ${}^4\text{He}$ nucleus, is one of the simplest and most stable nuclei, constituted by two protons and two neutrons. Its ground state features a spin-parity $J^\pi = 0^+$ and it is commonly indicated as the 0_1^+ state. Since its discovery [2], ${}^4\text{He}$ has captivated the scientific community as it represents the most stable nuclear system, which makes it the seed of clustering in light- to medium-mass nuclei [3] and of α -decay radioactivity

in heavy nuclei—the very same used by Rutherford. ${}^4\text{He}$ also plays a crucial role in astrophysics as a fundamental component of stellar matter and a vital element in stellar nucleosynthesis [4].

The modeling of ${}^4\text{He}$ in terms of 4 nucleons requires the solution of a quantum mechanical 4-body problem, where nuclear interactions are a key element. The task of solving for the ground-state could be achieved already in 2001 [5] by several so-called ab-initio methods [6]. Progress accomplished in the past two decades has been in increasing the precision of nuclear interactions (referred to as nuclear Hamiltonians), either in a phenomenological way [7, 8], or by introducing the more systematic effective field theory (EFT) approach, particularly in the variant based on chiral symmetry [9, 10]. Today, ground-state properties of ${}^4\text{He}$, such as binding energies and radii, are correctly described at about the percent level [11, 12], and even nuclei as heavy as ${}^{208}\text{Pb}$ [13] can be investigated by ab-initio nuclear theory. However, the description of the ${}^4\text{He}$ first excited state, a resonant state also featuring a spin-parity $J^\pi = 0^+$ and therefore commonly indicated as the 0_2^+ state, still represents a challenge. This state is, in fact, situated between the $p + {}^3\text{H}$ breakup channel starting at the proton-emission threshold $S_p = 19.813$ MeV, and the $n + {}^3\text{He}$ breakup channel demarcated by the neutron emission threshold S_n at 20.578 MeV.

The complication of computing such a state is intrinsic to its unbound resonant nature, as elucidated in a recent benchmark study [14]. The position E_r —typically indicated as the centroid-energy above the S_p threshold—and width Γ_r were calculated with various theories [14–20], obtaining quite different results depending on the method used and on the implemented nuclear force.

From an experimental perspective, determining the properties of the 0_2^+ state is also challenging. Inelastic scattering studies on ${}^4\text{He}$ targets using different projectiles, such as electrons [21–24], protons [25] and α -particles [26, 27], have in the past measured the position E_r and width Γ_r of this state. A large spread was observed, with a variation of about 0.6 and 0.7 MeV for E_r and Γ_r , respectively, and with some data being inconsistent with the other (see Fig. 1 and evaluation from Ref. [28]). Recently, the form factor F_M of the transition $0_1^+ \rightarrow 0_2^+$, connected by an electric monopole operator, has attracted much attention in the nuclear physics community, see [16, 19, 20, 29] and Supplementary Methods (1.2). As a matter of fact, calculations present stark differences, and none of them reproduces all the three known properties (E_r , Γ_r and F_M) of the 0_2^+ state. This is an unsatisfactory situation for what should be one of the best known nuclei. The properties of the first excited state of the α particle and their direct link to basic nuclear Hamiltonians are thus calling for further investigations.

Among the different probes which allow to populate the 0_2^+ state, inelastic scattering is the ideal toolbox as it requires minimal rearrangement of the ${}^4\text{He}$ nuclei. Nonetheless, notable differences arise depending on the projectiles employed in these studies. While electron scattering has the advantage of being perturbative, thus allowing for a direct connection of the cross section to the target properties, α scattering offers larger cross-sections, better state-selectivity and sensitivity to the density of the resonant state (see Supplementary Methods (1.1)), making it very effective for identifying resonant features, such as those of the 0_2^+ state in ${}^4\text{He}$. On the other hand, in the α - α scattering the many-body initial (ISI) and final state interactions (FSI)

need to be accurately modeled to get detailed information of the involved states. Although this procedure can affect the overall uncertainty of the data analysis, modern nuclear reaction methods are able to describe the cross section with enough accuracy to disentangle different nuclear structure theories. In this framework, the resulting uncertainties can be significantly reduced by constraining the ISI and FSI with supplementary measurements of other observables such as elastic scattering and total reaction cross section.

The main challenge in the description of the 0_2^+ state is its location in the continuum, where other excited states may overlap and/or interfere. Theoretical calculations [17] show that below 26 MeV of excitation energy (i.e., about 6 MeV above the S_p threshold) the relative angular momentum of the fragments is limited to $L = 0$ (S -wave) and $L = 1$ (P -wave). Nonetheless, a number of different partial waves, namely the 1S_0 , 3P_0 , 3P_1 , 3P_2 , may contribute. Here, the molecular notation $^{2S+1}L_J$ is adopted to label the ^4He states, where S is the quantum number relative to the sum of the spins of the two fragments (namely n and ^3He or p and ^3H), and $J(L)$ the total (orbital) angular momentum of the 4-body system. In addition, due to the $t = 1/2$ isospin of the two fragments, the ^4He excited states can either have isospin $T = 0$ (isoscalar) or $T = 1$ (isovector) quantum number. While in electron scattering all of these partial waves are involved, in α scattering only isoscalar $T = 0$ states with $S = 0, 1$ and $J = L$ can be populated. Therefore, besides the sought for 1S_0 resonance, only the 3P_1 partial wave located at 24.25 MeV contributes, making α scattering advantageous for our purposes.

Herein we report on a new study of the elastic and inelastic $\alpha + \alpha$ scattering at 53 MeV incident energy. The 0_2^+ resonance and a small portion of the spectrum above the resonance energy are investigated while keeping low the number of open reaction channels. In particular, the $\alpha + \alpha \rightarrow \alpha + p + ^3\text{H}$ and the $\alpha + \alpha \rightarrow \alpha + n + ^3\text{He}$ channels are experimentally accessed for the first time by exclusive experiments, making it possible to reconstruct the ^4He excitation energy with unprecedented low background, high resolution and selectivity. In this work we extract the energy and width of the 0_2^+ state from a modern analysis of a new α - α experiment (red point in Fig. 1), achieving the highly desired precision and providing a benchmark for future calculations.

While significant progress has recently been made in the *ab initio* treatment of nuclear reactions [30–35], no existing method can yet describe the inelastic α - α scattering process as an eight-body problem in the continuum. In this work, we model the process as a two coupled-channel system composed of the ground state 0_1^+ and the excited state 0_2^+ (treated as a bound state), with a $0_1^+ \rightarrow 0_2^+$ coupling channel. This approach is rooted in the well-established double-folding potential reaction theory. However, instead of using phenomenological densities as done in the traditional theory, we employ here state-of-the-art *ab initio* densities that stem from different nuclear Hamiltonians, the same used in analyzing electron scattering data. This represents a significant advance, and constitutes a solid framework for a first analysis of the $\alpha - \alpha$ scattering data presented here, that incorporates the microscopic physics presently available. Our analysis of the line shape of the 0_2^+ state and of the elastic and inelastic differential cross sections, indicates that densities from chiral EFT lead

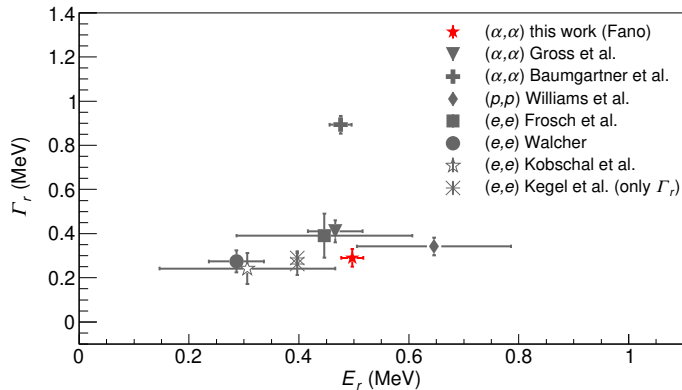


Fig. 1 Measured centroid-energy E_r and width Γ_r of the 0_1^+ resonance [21–27]. The E_r is defined with respect to the proton-emission threshold $S_p = 19.813$ MeV. The quoted error bars for the experimental datum of the present work (red) are discussed in Section 4.2.2. The error bars of the other data points are given in Refs. [21–27].

to a better agreement with experiment. However, space is left for an improvement of nuclear reaction models towards a full ab-initio description of the process.

2 Results

2.1 Experimental details

We performed an α -scattering experiment at the K800 Superconducting Cyclotron of the Istituto Nazionale di Fisica Nucleare – Laboratori Nazionali del Sud (INFN-LNS) in Catania (Italy), using a beam energy of 53 MeV. Thin metallic films with implanted ^4He atoms were used as targets. The ^4He ejectiles emitted at forward angles were detected by the MAGNEX magnetic spectrometer [36] while the ^3H and ^3He fragments from the decays of the populated ^4He excited state ($^4\text{He}^*$) were detected by the OSCAR array of solid state telescopes [37]. A schematic view of the set-up is given in Supplementary Fig. 1. The ejectiles were identified event by event in atomic number (Z), mass (A) and charge (see Methods 4.1 and Supplementary Fig. 2). The trajectories of the reaction ejectiles were then reconstructed and their momenta deduced at the target position (see Methods 4.2.1).

This set-up allows on the one hand to characterize the 0_2^+ resonance with unprecedented precision, and on the other hand, together with theoretical modeling, to provide stringent quality checks for ab-initio nuclear Hamiltonians.

2.2 The resonance characterization

In the inelastic process, the break-up channels $p + ^3\text{H}$ and $n + ^3\text{He}$ are experimentally accessed for the first time in hadronic experiments, making it possible to reconstruct the ^4He excitation energy with very low background, high resolution and selectivity.

Fig. 2 shows the reconstructed ${}^4\text{He}$ energy spectra from the $p + {}^3\text{H}$ (Fig. 2(a)) and $n + {}^3\text{He}$ (Fig. 2(b)) exit channels. In the $p + {}^3\text{H}$ the resonant 0_2^+ state is clearly populated over the non-resonant background, presenting an overall signal to background ratio of ≈ 12 . We describe the $p + {}^3\text{H}$ channel including: (i) the 1S_0 partial wave, featuring the resonant 0_2^+ state and the non-resonant breakup; (ii) the 3P_1 component, through the 1^- resonant state at 24.25 MeV ($E_r = 4.437$ MeV) [38]; (iii) the pick-up breakup processes $\alpha + \alpha \rightarrow {}^3\text{H} + {}^5\text{Li} \rightarrow \alpha + p + {}^3\text{H}$ centered at 21.78 MeV ($E_r = 1.967$ MeV), as it emerges from the results of transfer reaction simulations. Although this structure could partially overlap with the 0_2^+ state, we estimate an overall contribution of less than 0.2% in the region of the resonance between 19.72 and 20.84 MeV, which gives a negligible uncertainty in the 0_2^+ cross section once we subtract its yield.

For the $n + {}^3\text{He}$ channel we account for: (i) the 1S_0 non-resonant breakup (the 0_2^+ resonance is below the threshold for this channel); (ii) the 3P_1 resonance at 24.25 MeV ($E_r = 3.672$ MeV above the S_n threshold); (iii) the $\alpha + \alpha \rightarrow {}^3\text{He} + {}^5\text{He} \rightarrow \alpha + n + {}^3\text{He}$ pick-up break-up reaction.

In the $p + {}^3\text{H}$ channel, the interference of the 0_2^+ resonance with the 1S_0 non-resonant continuum and the presence of the tail of the 3P_1 partial wave clearly creates an asymmetry in the line shape. A powerful way to study such an interference was originally proposed by U. Fano [39] and progressively extended in the realm of modern physics [40–43]. Recently, it was used to characterize low-lying resonances in the ${}^{10}\text{Li}$ spectrum [44], inspiring us to use it also in the present study, leading to the very precise datum shown in Fig. 1. Upon implementing the Fano analysis (see details in Methods, section 4.2.2), E_r is found at 0.50 ± 0.02 MeV (corresponding to an excitation energy on top of the ground state of $E_x = 20.31 \pm 0.02$ MeV). Including the uncertainties, our result is found within the overlapping range of values from previous studies from electron scattering (0.29 - 0.45) and hadronic scattering (0.47 - 0.48). Remarkably, the maximum of the observed peak is at $E_r = 0.59$ ($E_x = 20.4$ MeV), which is about 0.1 MeV higher than the actual resonance centroid energy as a result of distortion in the line shape due to the interference. The extracted width Γ_r is 0.29 ± 0.04 MeV, in agreement with electron scattering studies but not with the α scattering analysis of Ref. [27], reporting 0.89 MeV. Instead, assuming a symmetric Lorentzian shape $E_r = 0.59 \pm 0.04$ and $\Gamma_r = 0.33 \pm 0.05$ are found. Thus, a systematic shift of about 90 keV for the resonance centroid and about 40 keV for the width is observed when the Lorentzian shape is adopted.

2.3 Angular-dependent cross section

Here, we perform new calculations for the elastic and inelastic scattering in the framework of the coupled channel quantum scattering theory and compare them to our experimental data. The ISI and FSI are built in a semi-microscopic approach by folding the nucleon-nucleon interaction with the 0_1^+ and 0_2^+ densities as well as the $0_1^+ \rightarrow 0_2^+$ transition density obtained from four different ab-initio calculations, all treating the 0_2^+ resonance as a bound state. The obtained ISI and FSI were validated through comparisons with elastic scattering and reaction cross section data (see Methods, section 4.4 for details). More details on the reaction modeling uncertainties can be found in section 4.4 and Supplementary Figs. 5, 6. First, we consider densities

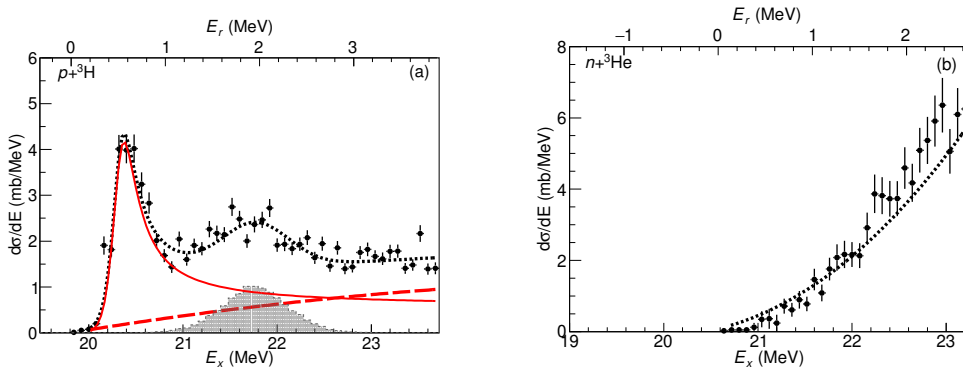


Fig. 2 Energy spectra for the $p + {}^3\text{H}$ and $n + {}^3\text{He}$ channels. (a) Experimental inelastic scattering spectrum (black dots) of the $p + {}^3\text{H}$ channel compared with the sum of three components (black dotted): 1S_0 (red solid), 3P_1 resonance at 24.25 MeV ($E_r = 4.437$ MeV) (red dashed) and $\alpha + \alpha \rightarrow {}^3\text{H} + {}^5\text{Li} \rightarrow \alpha + p + {}^3\text{H}$ pick-up break-up transfer (grey hatched area). (b) The $n + {}^3\text{He}$ channel, dominated by the simulated (black dotted) 3P_1 resonance at 24.25 MeV ($E_r = 3.672$ MeV). In both panels, error bars refer to the statistical and efficiency estimation uncertainties. The E_r (upper horizontal axis in top) refers to the centroid-energy above the S_p (a) and S_n (b) threshold, respectively.

from Bacca et al. [16, 45] and Viviani et al. [29], which use a chiral EFT Hamiltonian based on a two-body force at next-to-next-to-next-to leading order [46], and a different parametrization of the three-body force at next-to-next-to-leading order [47, 48]. We will display cross sections obtained from these two sets of densities in one band encompassing the differences and name it “the chiral EFT” family. Second, we consider densities obtained from calculations with two simplified Hamiltonians: one from Hiyama et al. [15], where the three-body force is purely central, and one from Meißner et al. [20], where the Hamiltonian is based on the $SU(4)$ isospin symmetry. We will display cross sections obtained from these two sets of densities as a band encompassing the differences and denote it as the “simplified Hamiltonian” family. These two bands serve as an uncertainty estimate quantifying the dependence of the cross section on the input densities.

Fig. 3 shows the experimental angular distributions of the differential cross section in comparison to theoretical calculations. On panel (a) we have our experimental data obtained at a beam energy of 53 MeV, while on the panel (b) we also show previously published data at a beam energy of 64 MeV [26]. In both cases, we consider only the contribution of the 0_2^+ resonance extracted, angle by angle, from the peaked spectral shape centered at 20.4 MeV, after a polynomial modeling of the background underneath. This accounts in average for the 3P_1 as well as the 1S_0 non-resonant and interference contributions.

A fair agreement is found between the data and the calculations adopting the chiral EFT densities, both at 53 and 64 MeV. The pronounced minimum present in the data at 64 MeV at $\theta_{c.m.} \approx 18^\circ$ (corresponding to $q \approx 0.85 \text{ fm}^{-1}$) is well reproduced. However, no clear sign of the minimum observed at 53 MeV at $\theta_{c.m.} \approx 23^\circ$ is present in

the calculations. Differently from chiral EFT calculations, results from the simplified Hamiltonian family deviate from the data at 53 MeV as well as at small angles for the 64 MeV energy. At large angles for 64 MeV, all theories predict a minimum at $\theta_{c.m.} \approx 65^\circ$ but the data are significantly less accurate there.

Confronting the experimental inelastic cross sections at 53 MeV and 64 MeV incident energy a marked difference appears, especially in the region at low momentum transfer. Indeed, due to the high excitation energy, the population of the 0_2^+ state also determines a sudden change of the kinetic energy and wavelength for the colliding systems. This unveils an interesting situation where a small change in the projectile energy generates a substantial change in the diffraction pattern, paving the way for a strong sensitivity of this process to fine details of the scattering dynamics, namely the spatial distributions of the ^4He 0_1^+ and 0_2^+ states. The pronounced first minimum observed at $\approx 0.85 \text{ fm}^{-1}$ for the cross section at 64 MeV energy is damped at 53 MeV and shifted at $\approx 0.95 \text{ fm}^{-1}$, while it almost disappears in the calculations.

An expansion of the calculated inelastic scattering cross sections in terms of the angular momentum l of the relative motion of the outgoing nuclei allows to get insight on this situation. At 64 MeV the cross section is mainly fed by the $l = 4$ partial wave, with minor role for the $l = 0$ and $l = 2$ and negligible contribution for $l \geq 6$. The $l = 4$ partial wave features a pronounced minimum at about 20° , common to all calculations as well as to the data. Instead, the $l = 2$ contribution is the leading one at 53 MeV, also due to the less available momentum for the scattering waves, with a minimum at about 55° and a growing trend down to zero degree. In the case of the simplified Hamiltonian, the same analysis still indicates a similar behavior at both the energies, although the $l = 4$ contribution at 53 MeV is more relevant and a minimum starts to appear at forward angles ($\approx 15^\circ$). As a consequence, the data at 53 MeV suggest the need for a mild redistribution of the cross section partial waves toward an enhanced $l = 4$ contribution. In terms of radial distribution of the cross section this shift toward larger l reflects the need of more density overlap of the two colliding nuclei at larger distances ($R \gtrsim 4 \text{ fm}$). This is significantly larger than the size of ^4He ground state radius ($r(^4\text{He}_{g.s.}) = 1.7 \text{ fm}$ [49]), typically explored in electron scattering experiments indicating that with α scattering we are probing more peripheral regions of the density. In particular, while the latter is sensitive only to the transition density, α - α scattering is particularly sensitive to the density of the 0_2^+ excited state, for which the prediction of the four different ab-initio calculations differ substantially.

We find that the best result is given by the chiral EFT density by Viviani et al. [29] and prove that inelastic α - α scattering poses stringent tests to nuclear structure models, emphasized by the strong sensitivity of the diffractive patterns in the cross section angular distributions to the details of the resonances density profile.

3 Discussion

Our study allows to give insight on the nature of the 0_2^+ resonance of ^4He and provides strong constraints for present and future models of the nuclear Hamiltonian. The adopted experimental technique allowed to get an unprecedented clean and background-free spectral response. Our results within the Fano theory of resonances

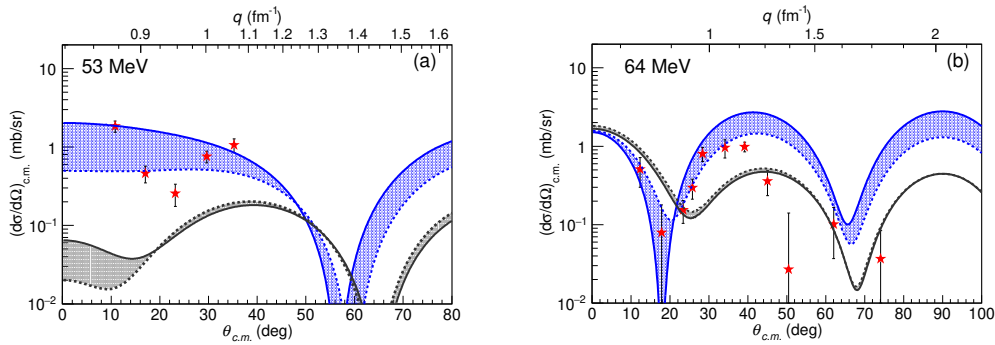


Fig. 3 Inelastic scattering angular distributions. Inelastic scattering differential cross section for the 0_2^+ resonance as a function of the scattering angle in the centre-of-mass frame (lower horizontal axis) or the momentum transfer (upper horizontal axis) at 53 MeV (a) and 64 MeV [26] (b) incident beam energy. The experimental data (red stars) are compared with the theoretical results obtained using the (blue band) chiral effective field theory densities (solid [16] and dashed [29]) and the (grey band) simplified Hamiltonian densities (solid [20] and dashed [15]). The error bars correspond to the combination of uncertainties coming from the solid angle and detection efficiency estimation, the uncertainties in the beam current and the target thickness determination, the statistical error and the background subtraction. See text for details.

give a centroid energy of $E_r = 0.50 \pm 0.02$ MeV and a width $\Gamma_r = 0.29 \pm 0.04$ MeV, providing the most precise ever measurements of the 0_2^+ resonance, in disagreement with previous α -scattering data [26, 27] but in agreement, as for the width, with the latest electron scattering experiment by Kegel et al. [24]. Since the Fano analysis indicates a significant interference between the 0_2^+ resonance and the underlying non resonant continuum, employing a similar analysis on other scattering data would be interesting.

The comparisons of the experimental cross sections with calculations based on coupled channels quantum scattering theory, with ab-initio densities used in input, has allowed to set a robust test of ^4He wave functions of the ground state 0_1^+ , the 0_2^+ resonance, and the $0_1^+ \rightarrow 0_2^+$ transition density. Interestingly, we find that densities from chiral EFT better describe the α scattering data. Due to the importance of the 0_2^+ density in the $\alpha - \alpha$ scattering calculation, we conclude that while the densities from Refs.[15, 20] well reproduce the transition form factor probed by electron scattering, they do not well describe the density of the excited state probed by the α scattering. The chiral densities of Viviani et al. [29] provide the best overall agreement with data from both electron and α scattering, despite a slight deviation from the diffraction pattern observed in α scattering at 53 MeV.

At the same time, the fact that the interaction used in Ref. [29] predicts a resonance position and width that deviate from the experimentally extracted values (see Fig. 1) highlights a deeper challenge. Indeed, establishing a transparent link between the measured cross section in an open quantum system, such as α - α scattering and the underlying resonance in one of its sub-systems, remains a challenging

problem in quantum mechanics. Despite notable advances in reaction theory, a fully quantitative framework applicable to inelastic α - α scattering is still lacking. Our analysis—based on a robust yet necessarily approximate and not fully consistent reaction model—demonstrates that combining α -scattering with electron-scattering substantially tightens the sensitivity to the underlying microscopic physics. These results not only expose the current theoretical limitations but also clearly define the direction for future progress, including the long-term goal of constructing an ab-initio optical potential for light nuclei. Ultimately, the high-precision data reported here, together with the insights gained from this study, provide a compelling impetus for advancing theoretical approaches to inelastic α - α scattering.

4 Methods

4.1 Experimental set-up and particle identification

Two experiments were performed at the MAGNEX facility [36] of the Istituto Nazionale di Fisica Nucleare – Laboratori Nazionali del Sud (INFN-LNS) in Catania.

The first experiment was dedicated to the elastic scattering measurement in the angular range $6.5^\circ \leq \theta_{\text{Lab}} \leq 45^\circ$, corresponding to $13^\circ \leq \theta_{\text{c.m.}} \leq 90^\circ$ in the centre of mass reference frame. The ^4He beam was accelerated by the K800 Superconducting Cyclotron at 53 MeV (13.2 MeV/u) incident energy and impinged on a solid target, built by the implantation of ^4He atoms on a ^{181}Ta sheet. The effective thickness of ^4He component of the target, measured by Rutherford back-scattering (RBS) technique, was $2.5 \pm 0.13 \mu\text{g cm}^{-2}$ (3.7×10^{17} atoms cm^{-2}) while the thickness of ^{181}Ta was $950 \pm 10 \mu\text{g cm}^{-2}$ (3.2×10^{18} atoms cm^{-2}). Residual impurities of oxygen ($14.6 \pm 0.4 \mu\text{g cm}^{-2}$ (5.5×10^{17} atoms cm^{-2})) were observed in the RBS analyses. The beam current was measured by a Faraday cup (FC) mounted 15 cm downstream of the target. The solid angle of MAGNEX was 50 msr, defined by four 1 mm thick tantalum slits located 25 cm downstream of the target. The α -particle ejectiles were detected by the MAGNEX Focal Plane Detector (FPD) [50], which consists of a gas-filled tracker followed by a wall of 60 ($5 \times 7 \text{ cm}^2$ area, 1 mm thick) silicon pad detectors.

In the second experiment, conducted at the same facility, the inelastic scattering was studied by performing a coincidence measurement between the ^4He ejectiles and one of the breakup fragments emitted by the residual ^4He (^3H or ^3He). Our study was designed such as to explore a significant portion of the phase space for both the $^3\text{H} + p$ and $^3\text{He} + n$ decay modes. The experimental set-up is illustrated in Supplementary Fig. 1. Additional elastic scattering data were collected under experimental conditions similar to the first experiment to cross check. The ^4He beam was accelerated at 53 MeV incident energy and impinged on a solid target built by the implantation of ^4He atoms on a ^{27}Al sheet. The replacement of the tantalum backing with an aluminium one was intended to further reduce the background observed in the first experiment, attributed to beam scattering on tantalum. The effective thickness of ^4He was $1.3 \pm 0.1 \mu\text{g cm}^{-2}$ (1.9×10^{17} atoms cm^{-2}) while the thickness of ^{27}Al was $210 \pm 2 \mu\text{g cm}^{-2}$ (4.6×10^{18} atoms cm^{-2}). Residual impurities of oxygen ($2.7 \pm 0.1 \mu\text{g cm}^{-2}$ (1.0×10^{17} atoms cm^{-2})) and carbon ($0.2 \pm 0.02 \mu\text{g cm}^{-2}$ (1.2×10^{16} atoms cm^{-2})) were observed in the RBS analyses. The beam current was measured by a FC

mounted 15 cm downstream of the target. The measurement was repeated with an ancillary target composed of aluminium, oxygen and carbon in the appropriate proportions for background estimation. The ^4He ejectiles were momentum analysed by the MAGNEX spectrometer, whose optical axis was set at $\theta_{\text{opt}} = 6.6^\circ$, spanning the range of detection angles between $2^\circ \leq \theta_{\text{Lab}} \leq 12^\circ$ in the laboratory reference frame. The momentum acceptance of the spectrometer ($\approx 24\%$) [36] allowed the measurement of the ^4He excitation energy (E_x) up to 4.0 MeV above the S_p threshold, covering a significant part of the available energy spectrum, which extends up to 6.7 MeV above S_p at the beam energy of the experiment. The α -particle ejectiles were detected by the MAGNEX FPD, while the ^3H and ^3He fragments were detected by the OSCAR solid state telescope ($5 \times 5 \text{ cm}^2$ area) [37]. This device consists of two detection stages: a Single Sided Silicon Strip Detector (SSSSD), which measures the energy loss ΔE , followed by 16 Silicon pads (arranged in a 4×4 mode) for measuring the ions residual energy E_{resid} . The thicknesses of $20 \mu\text{m}$ for the ΔE and $300 \mu\text{m}$ for the E_{resid} allow the unambiguous identification of light reaction fragments with energies of few MeV. In particular, the energy range of ^3H and ^3He particles detected by OSCAR was 2.5 - 9.0 MeV and 5.0 - 11.2 MeV, respectively. For both of them a large part of their phase space was explored. The OSCAR system was mounted inside the MAGNEX scattering chamber, 15 cm far from the target, subtending an angular range between 19° and 38° with an angular resolution of $\sim 1^\circ$. The unambiguous particle identification is illustrated in Supplementary Fig. 2. Details on the particle identification technique can be found at Refs. [37, 51].

4.2 Details of data reduction

4.2.1 Energy spectra

The trajectories of the ^4He ejectiles detected at the MAGNEX FPD were reconstructed and the momentum vector was deduced at the target position, adopting the methodology described in Ref. [52]. The missing mass technique, with the use of relativistic kinematics relations, was adopted to get ^4He energy spectra. The inelastic scattering events were further characterized by the coincident measurement of ^3H or ^3He fragments by the OSCAR telescope (see section 4.2.3). The obtained energy resolution, in the region of the $^4\text{He}(0_2^+)$ state, ranges from $\delta_E \approx 80 \text{ keV}$ at small scattering angles to $\delta_E \approx 100 \text{ keV}$ for the largest explored angles. This was mainly determined by the spectrometer response, the beam energy spreading and the kinematic energy dependence on the scattering angle. A weighted energy resolution of 86 keV was estimated when summing the spectra of all explored angles.

4.2.2 Line shape analysis

An important aspect in analyzing the $^4\text{He}(0_2^+)$ resonance is to include the contribution of the $L > 0$ resonant and non-resonant strengths and the possible interference between the 0_2^+ resonance with the underlying non-resonant continuum featuring the same 0^+ quantum numbers. A powerful way to study this topic was proposed by Fano [39], stemming from the asymmetric line shape (modeled by the Fano function) generated by such interference.

An additional feature is the distortion of the resonance line shape due to the proximity of the particle emission threshold [53]. Since the strength is zero below the threshold an asymmetric line shape is always found, although the actual shape depends also on the multipolarity. Differently from the Fano asymmetry, the threshold effect does not depend on the dynamic mechanism populating the resonance, thus providing a stable distortion of its line shape. The stronger is the distortion the larger is $\Delta_r = \Gamma_r / (E_r - E_t)$, the ratio between the resonance full width at half maximum (Γ_r) and the distance of the resonance centre (E_r) from the threshold (E_t), especially when Δ_r exceeds unity. In the $p + {}^3\text{H}$ channel the threshold at $S_p = 19.813$ MeV can affect the line shape for both the 1S_0 ($\Delta_r \approx 0.7$) and the isoscalar 3P_1 ($\Delta_r \approx 1.4$) resonances, with a smaller impact on the former thanks to its smaller width. Ideally, both the interference with non-resonant continuum and the threshold effect should be included in the resonance line shape analysis. However, to our knowledge such a theoretical framework is not available to date and approximate schemes are needed.

Our assumption for the 1S_0 resonance is to account only for the Fano asymmetry, since $\Delta_r < 1$. In reverse, we assume only the threshold effect for the isoscalar 3P_1 , considering the small $L = 1$ non-resonant strength in the explored excitation energy region [17]. Fig. 2 (a) shows the best fit obtained adopting a Fano function, convoluted with experimental energy resolution, as a model of the observed structure in the region of the 0_2^+ state. In this framework the cross section in the region of the resonance is given as

$$\sigma = \sigma_{cont} \frac{|q_F + \epsilon|^2}{1 + \epsilon^2}, \quad (1)$$

where σ_{cont} is the inelastic cross section of the non-resonant continuum and $\epsilon = 2(E - E_r)/\Gamma_r$, where E_r is the resonance centre and Γ_r its width. The line shape is controlled by the Fano parameter q_F which, apart from a phase factor, is determined by the relative weight of the resonant and non-resonant amplitudes. An interesting aspect of the Fano theory is that the q_F parameter depends on the dynamics of the resonance population, while the resonance centre and width do not change. When $q_F \gg 1$ the line shape becomes progressively more symmetric approaching the Lorentzian function when q_F goes to infinite. For this analysis, we find $q_F = 2.54 \pm 0.07$ when we consider the spectrum in the full explored angular region, which calls for a significant effect from the interference discussed here. Further analyses of the line shape in smaller angular slices of the measured cross section do reveal that the resonance centre and width are stable, within the quoted uncertainties.

The quoted uncertainties for the resonance energy (± 0.02 MeV) and width (± 0.04 MeV) include the uncertainty in the energy threshold effect on the line shape model, the deconvolution of the spectrum in the three components (as shown in Fig. 2), the contribution of the finite bin size, the accuracies in energy or/and angle of the delivered beam, the spectrometer and the ray-reconstruction procedure as well as the variation of the experimental resolution as a function of angle (see Methods (4.2.1)).

4.2.3 Cross section determination

The elastic scattering yields were determined with angular steps of 0.5° in MAGNEX over the explored angular range. The differential cross-section was extracted through

a careful determination of the experimental yield, the beam flux, the target thickness, the explored solid angle and the detection efficiency. For the inelastic scattering process, exclusive yields were determined with angular steps of 2° in MAGNEX, combined with the whole OSCAR system, to reach a compromise with the reduced yield of the coincidence measurement. The background due to aluminium, oxygen and carbon impurities in the target as well as that generated by spurious signals in the detectors was negligible in the coincidence spectra, leading to an overall signal to instrumental background ratio ranging between 15 and 40 at the different detection angles. Nonetheless, this background was experimentally determined using data collected with the ancillary target and subtracted.

The efficiency of our detection system in the coincidence measurement was calculated by the MULTIP Monte Carlo simulation algorithm [54], taking into account the MAGNEX intrinsic efficiency [55]. The exclusive yields, corrected for the detection efficiency, were transformed to laboratory double differential cross sections taking into account the areal density of the ^4He scattering centres, the beam current, the MAGNEX and OSCAR solid angles, the last one computed by a Monte Carlo simulation.

4.3 Calculation methodology

The theoretical cross section angular distributions were calculated in the coupled - channel quantum scattering theory framework. The nucleus - nucleus potential was obtained by double folding the nucleon - nucleon interaction with densities from four different ab-initio theories. A first group consisted by two theories of the chiral EFT family by Bacca et al. [16, 45] and Viviani et al. [29] while, a second one, by theories on which the densities were obtained from calculations with two simplified Hamiltonians by Hiyama et al. [15] and by Meißner et al. [20]. The $\rho_{0_1^+}$ and $\rho_{0_2^+}$ densities for the 0_1^+ and 0_2^+ state respectively, as well the transition density $\rho_{0_1^+ \rightarrow 0_2^+}$ are presented in Supplementary Fig. 3(a-c). One can find more details on the reaction theory, the double folding model and the densities in Supplementary Methods (1.1), on the adopted potentials in the reaction theory in Supplementary Methods (1.1.1) and on the used ab-initio theory in Supplementary Methods (1.2). Finally, in Supplementary Methods (1.2.1), one may see how we successfully handle the 0_2^+ lying in the continuum as an effective bound state. The reliability of the process is illustrated in Supplementary Fig. 3(d). The calculated centroid-energy, assuming the 0_2^+ as an effective bound state, is $E_r = 0.5 \pm 0.1$ MeV.

4.4 Assessment of the reaction modeling uncertainties

As for the uncertainties in the reaction modeling, the main source comes from limitations in the adopted model space and uncertainties in the determination of the ISI and FSI. Indeed, our coupled - channel reaction scheme includes explicitly only the elastic scattering and the inelastic excitation of the 0_2^+ resonance. Other inelastic channels, although kinematically accessible, are accounted for in average through a complex polarization nucleus - nucleus potential. A phase - shift analysis with the adopted potentials was performed as described in Supplementary Methods (1.1.1),

whose results are illustrated in Supplementary Fig. 4. The availability of a rich and accurate dataset at ${}^4\text{He} + {}^4\text{He}$ interaction at different energies and for different partial waves [56–65] gave us the chance to fine tune the potential and evaluate a realistic uncertainty band. In particular, the range of the band was set in order to allow variations of the $|S|$ matrix within an interval $\Delta|S| = \pm 0.1$ around the best value. The goodness of this approach is first evaluated through comparisons of the calculated elastic scattering angular distribution cross sections at $E_{Lab} = 53$ MeV with our data as shown in Supplementary Fig. 5 (a), presenting an overall good agreement. The existing elastic scattering data at 53.4 MeV from Ref. [65] are also in good agreement with the new dataset. Our theoretical framework has been adopted to analyze also the existing elastic scattering data at $E_{Lab} = 64$ MeV from Ref. [65]. Remarkably, the theoretical results are in very good agreement with these data as visible in Supplementary Fig. 5 (b). Overall, the results point to a strong reliability of our phase shift analysis and consequently of our ISI. Further comparisons were performed between the total reaction cross section (σ_{tot}^{theo}), from coupled-channel calculations with that extracted from suitable experimental data and reliable fusion reaction calculations (σ_{tot}^{exp}) [66–68]. The σ_{tot} observable is notoriously related to the imaginary part of the ISI. The result of this comparison is presented in Supplementary Table 1, presenting a very good agreement between experimental (σ_{tot}^{exp}) and theoretical (σ_{tot}^{theo}) reaction cross sections, although the error bars are sizable in both cases. The effect of the nucleon - nucleon interaction was found negligible by changing the adopted Brazilian Nuclear Potential (BNP) with the Hamiltonians used in the ab-initio densities.

Finally, the effect of the uncertainty band in the ${}^4\text{He} + {}^4\text{He}$ interaction in the inelastic angular distribution cross sections is presented in Supplementary Fig. 6.

Data availability. The data are available from the corresponding author upon reasonable request.

References

- [1] Rutherford, E. The scattering of α and β particles by matter and the structure of the atom. *The London, Edinburgh, and Dublin Philosophical Magazine and Journal of Science* **21**, 669–688 (1911). URL <https://doi.org/10.1080/14786440508637080>.
- [2] News. The British Association Meeting at Edinburgh. *Nature* **4**, 261–278 (1871). URL <https://doi.org/10.1038/004261a0>.
- [3] Freer, M. Clusters in nuclei. *Scholarpedia (Ed. N. Alamanos)* **5**, 9652 (2010). URL <http://dx.doi.org/10.4249/scholarpedia.9652>.
- [4] Iliadis, C. *Nuclear Physics of Stars* (Wiley, Weinheim, 2007).
- [5] Kamada, H. *et al.* Benchmark test calculation of a four-nucleon bound state. *Phys. Rev. C* **64**, 044001 (2001).

- [6] Ekström, A. *et al.* What is ab initio in nuclear theory? *Frontiers in Physics* **11** (2023). URL <https://www.frontiersin.org/journals/physics/articles/10.3389/fphy.2023.1129094>.
- [7] Pudliner, B. S., Pandharipande, V. R., Carlson, J. & Wiringa, R. B. Quantum monte carlo calculations of $A \leq 6$ nuclei. *Phys. Rev. Lett.* **74**, 4396–4399 (1995). URL <https://link.aps.org/doi/10.1103/PhysRevLett.74.4396>.
- [8] Wiringa, R. B., Stoks, V. G. J. & Schiavilla, R. Accurate nucleon-nucleon potential with charge-independence breaking. *Phys. Rev. C* **51**, 38–51 (1995). URL <https://link.aps.org/doi/10.1103/PhysRevC.51.38>.
- [9] Epelbaum, E., Hammer, H.-W. & Meißner, U.-G. Modern Theory of Nuclear Forces. *Rev. Mod. Phys.* **81**, 1773–1825 (2009).
- [10] Hammer, H.-W., König, S. & van Kolck, U. Nuclear effective field theory: Status and perspectives. *Rev. Mod. Phys.* **92**, 025004 (2020). URL <https://link.aps.org/doi/10.1103/RevModPhys.92.025004>.
- [11] Maris, P. *et al.* Light nuclei with semilocal momentum-space regularized chiral interactions up to third order. *Phys. Rev. C* **103**, 054001 (2021). URL <https://link.aps.org/doi/10.1103/PhysRevC.103.054001>.
- [12] Kievsky, A., Rosati, S., Viviani, M., Marcucci, L. & Girlanda, L. A High-precision variational approach to three- and four-nucleon bound and zero-energy scattering states. *J. Phys. G* **35**, 063101 (2008).
- [13] Hu, B. *et al.* Ab initio predictions link the neutron skin of ^{208}Pb to nuclear forces. *Nature Phys.* **18**, 1196–1200 (2022).
- [14] Duerinck, P.-Y. *et al.* Excited state of the α particle: A benchmark study. *Phys. Rev. C* **112**, 044001 (2025). URL <https://link.aps.org/doi/10.1103/jcd4-8jh8>.
- [15] Hiyama, E., Gibson, B. F. & Kamimura, M. Four-body calculation of the first excited state of ^4He using a realistic nn interaction: $^4\text{He}(e, e')^4\text{He}(0_2^+)$ and the monopole sum rule. *Phys. Rev. C* **70**, 031001 (2004). URL <https://link.aps.org/doi/10.1103/PhysRevC.70.031001>.
- [16] Bacca, S., Barnea, N., Leidemann, W. & Orlandini, G. Isoscalar monopole resonance of the alpha particle: A prism to nuclear hamiltonians. *Phys. Rev. Lett.* **110**, 042503 (2013). URL <https://link.aps.org/doi/10.1103/PhysRevLett.110.042503>.
- [17] Viviani, M., Girlanda, L., Kievsky, A. & Marcucci, L. E. $n + ^3\text{H}$, $p + ^3\text{He}$, $p + ^3\text{H}$, and $n + ^3\text{He}$ scattering with the hyperspherical harmonic method. *Phys. Rev. C* **102**, 034007 (2020). URL <https://link.aps.org/doi/10.1103/PhysRevC.102.034007>.

- [18] Aoyama, S. A theoretical treatment of four-body resonances by using the complex scaling method. *Progress of Theoretical and Experimental Physics* **2016**, 123D01 (2016). URL <https://doi.org/10.1093/ptep/ptw171>.
- [19] Michel, N., Nazarewicz, W. & Płoszajczak, M. Description of the proton-decaying 0_2^+ resonance of the α particle. *Phys. Rev. Lett.* **131**, 242502 (2023). URL <https://link.aps.org/doi/10.1103/PhysRevLett.131.242502>.
- [20] Meißner, U.-G., Shen, S., Elhatisari, S. & Lee, D. Ab initio calculation of the alpha-particle monopole transition form factor. *Phys. Rev. Lett.* **132**, 062501 (2024). URL <https://link.aps.org/doi/10.1103/PhysRevLett.132.062501>.
- [21] Frosch, R. *et al.* Inelastic electron scattering from ^4He . *Nuclear Physics A* **110**, 657–673 (1968). URL <https://www.sciencedirect.com/science/article/pii/0375947468903795>.
- [22] Walcher, T. Excitation of ^4He by inelastic electron scattering at low momentum transfer. *Physics Letters B* **31**, 442–444 (1970). URL <https://www.sciencedirect.com/science/article/pii/0370269370901486>.
- [23] Köbschall, G. *et al.* Excitation of the quasi-bound state in ^4He by electron scattering at medium momentum transfer. *Nuclear Physics A* **405**, 648–652 (1983). URL <https://www.sciencedirect.com/science/article/pii/0375947483905237>.
- [24] Kegel, S. *et al.* Measurement of the α -particle monopole transition form factor challenges theory: A low-energy puzzle for nuclear forces? *Phys. Rev. Lett.* **130**, 152502 (2023). URL <https://link.aps.org/doi/10.1103/PhysRevLett.130.152502>.
- [25] Williams, L. E. Continuum resonances in $\text{He}^4(p, p')\text{He}^{4*}$. *Phys. Rev.* **144**, 815–822 (1966). URL <https://link.aps.org/doi/10.1103/PhysRev.144.815>.
- [26] Gross, E. E., Hungerford, E. V., Malanify, J. J., Pugh, H. G. & Watson, J. W. Investigation of the reaction $^4\text{He} (^4\text{He}, ^4\text{He}) ^4\text{He}^*$ at 64 MeV. *Phys. Rev.* **178**, 1584–1590 (1969). URL <https://link.aps.org/doi/10.1103/PhysRev.178.1584>.
- [27] Baumgartner, M. *et al.* The α^* and the neutron scattering lengths of ^3He . *Nuclear Physics A* **368**, 189–200 (1981). URL <https://www.sciencedirect.com/science/article/pii/0375947481906813>.
- [28] Tilley, D., Weller, H. & Hale, G. Energy levels of light nuclei $A = 4$. *Nuclear Physics A* **541**, 1–104 (1992).
- [29] Viviani, M., Kievsky, A., Marcucci, L. E. & Girlanda, L. Study of the alpha-particle monopole transition form factor. *Few Body Systems* **65**, 74 (2024). URL <https://doi.org/10.1007/s00601-024-01940-2>.
- [30] Elhatisari, S. *et al.* Ab initio alpha–alpha scattering. *Nature* **528**, 111–114 (2015).

- [31] Elhatisari, S., Hildenbrand, F. & Meißner, U.-G. Ab initio lattice study of neutron-alpha scattering with chiral forces at N3LO (2025). URL <https://arxiv.org/abs/2507.08495>. arXiv:2507.08495.
- [32] Idini, A., Barbieri, C. & Navrátil, P. Ab initio optical potentials and nucleon scattering on medium mass nuclei. *Phys. Rev. Lett.* **123**, 092501 (2019).
- [33] Mercenne, A., Michel, N., Fernández, J. P. L. & Płoszajczak, M. Gamow shell model description of the $^{40}\text{Ca}(d,p)$ transfer reaction. *Phys. Rev. C* **107**, L011603 (2023).
- [34] Kravvaris, K., Quaglioni, S., Hupin, G. & Navrátil, P. Ab initio framework for nuclear scattering and reactions induced by light projectiles. *Physics Letters B* **856**, 138930 (2024).
- [35] Rotureau, J., Danielewicz, P., Hagen, G., Nunes, F. M. & Papenbrock, T. Optical potential from first principles. *Phys. Rev. C* **95**, 024315 (2017).
- [36] Cappuzzello, F., Agodi, C., Carbone, D. & Cavallaro, M. The MAGNEX spectrometer: Results and perspectives. *Eur. Phys. J. A* **52**, 167 (2016). URL <https://doi.org/10.1140/epja/i2016-16167-1>.
- [37] Dell’Aquila, D. *et al.* OSCAR: A new modular device for the identification and correlation of low energy particles. *Nuclear Instruments and Methods in Physics Research Section A: Accelerators, Spectrometers, Detectors and Associated Equipment* **877**, 227–237 (2018).
- [38] Harakeh, M. N. & van der Woude, A. *Giant Resonances: Fundamental High-Frequency Modes of Nuclear Excitation* (Oxford University Press, Oxford, 2001).
- [39] Fano, U. Effects of configuration interaction on intensities and phase shifts. *Phys. Rev.* **124**, 1866–1878 (1961). URL <https://link.aps.org/doi/10.1103/PhysRev.124.1866>.
- [40] Luk’Yanchuk, B. *et al.* The Fano resonance in plasmonic nanostructures and metamaterials. *Nature Materials* **9**, 707 – 715 (2010).
- [41] Ott, C. *et al.* Lorentz meets Fano in spectral line shapes: A universal phase and its laser control. *Science* **340**, 716–720 (2013). URL <https://www.science.org/doi/abs/10.1126/science.1234407>.
- [42] Limonov, M., Rybin, M., Poddubny, A. & Kivshar, Y. Fano resonances in photonics. *Nature Photonics* **11**, 543–554 (2017). URL <https://doi.org/10.1038/nphoton.2017.142>.
- [43] Paliwal, P., Blech, A., Koch, C. P. & Narevicius, E. Fano interference in quantum resonances from angle-resolved elastic scattering. *Nature Communications* **12**,

7249 (2021).

- [44] Cavallaro, M. *et al.* Investigation of the ^{10}Li shell inversion by neutron continuum transfer reaction. *Phys. Rev. Lett.* **118**, 012701 (2017). URL <https://link.aps.org/doi/10.1103/PhysRevLett.118.012701>.
- [45] Bacca, S., Barnea, N., Leidemann, W. & Orlandini, G. Examination of the first excited state of ^4He as a potential breathing mode. *Phys. Rev. C* **91**, 024303 (2015). URL <https://link.aps.org/doi/10.1103/PhysRevC.91.024303>.
- [46] Entem, D. R. & Machleidt, R. Accurate charge-dependent nucleon-nucleon potential at fourth order of chiral perturbation theory. *Phys. Rev. C* **68**, 041001 (2003). URL <https://link.aps.org/doi/10.1103/PhysRevC.68.041001>.
- [47] Navrátil, P. Local three-nucleon interaction from chiral effective field theory. *Few-Body Systems* **41**, 117 (2007). URL <https://doi.org/10.1007/s00601-007-0193-3>.
- [48] Baroni, A. *et al.* Local chiral interactions, the tritium Gamow-Teller matrix element, and the three-nucleon contact term. *Phys. Rev. C* **98**, 044003 (2018).
- [49] Wang, R., Han, C. & Chen, X. Exploring the mass radius of ^4He and implications for nuclear structure. *Phys. Rev. C* **109**, L012201 (2024). URL <https://link.aps.org/doi/10.1103/PhysRevC.109.L012201>.
- [50] Torresi, D. *et al.* An upgraded focal plane detector for the MAGNEX spectrometer. *Nuclear Instruments and Methods in Physics Research Section A: Accelerators, Spectrometers, Detectors and Associated Equipment* **989**, 164918 (2021). URL <https://www.sciencedirect.com/science/article/pii/S0168900220313152>.
- [51] Cappuzzello, F. *et al.* A particle identification technique for large acceptance spectrometers. *Nuclear Instruments and Methods in Physics Research Section A: Accelerators, Spectrometers, Detectors and Associated Equipment* **621**, 419–423 (2010). URL <https://www.sciencedirect.com/science/article/pii/S0168900210011241>.
- [52] Cappuzzello, F., Carbone, D. & Cavallaro, M. Measuring the ions momentum vector with a large acceptance magnetic spectrometer. *Nuclear Instruments and Methods in Physics Research Section A: Accelerators, Spectrometers, Detectors and Associated Equipment* **638**, 74–82 (2011). URL <https://www.sciencedirect.com/science/article/pii/S0168900211003585>.
- [53] McVoy, K. & Van Isacker, P. Does the ground-state resonance of ^{10}Li overlap neutron threshold? *Nuclear Physics A* **576**, 157–164 (1994).
- [54] O. Sgouros, V. Soukeras & A. Pakou. Multip : A multi purpose simulation monte carlo algorithm for two- and three-body reaction kinematics. *Eur. Phys. J. A* **53**, 165 (2017). URL <https://doi.org/10.1140/epja/i2017-12359-5>.

- [55] Cavallaro, M. *et al.* Transport efficiency in large acceptance spectrometers. *Nuclear Instruments and Methods in Physics Research Section A: Accelerators, Spectrometers, Detectors and Associated Equipment* **637**, 77–87 (2011).
- [56] Russell, J. L., Phillips, G. C. & Reich, C. W. Scattering of alpha particles from helium. *Phys. Rev.* **104**, 135–142 (1956). URL <https://link.aps.org/doi/10.1103/PhysRev.104.135>.
- [57] Heydenburg, N. P. & Temmer, G. M. Alpha-alpha scattering at low energies. *Phys. Rev.* **104**, 123–134 (1956). URL <https://link.aps.org/doi/10.1103/PhysRev.104.123>.
- [58] Nilson, R., Kerman, R. O., Briggs, G. R. & Jentschke, W. Alpha-alpha particle scattering in the energy range 12.3 to 22.9 MeV. *Phys. Rev.* **104**, 1673–1680 (1956). URL <https://link.aps.org/doi/10.1103/PhysRev.104.1673>.
- [59] Bacher, A. D. *et al.* Observation of high-lying levels in ^8Be from $\alpha - \alpha$ elastic scattering. *Phys. Rev. Lett.* **29**, 1331–1333 (1972). URL <https://link.aps.org/doi/10.1103/PhysRevLett.29.1331>.
- [60] Tombrello, T. A. & Senhouse, L. S. Elastic scattering of alpha particles from helium. *Phys. Rev.* **129**, 2252–2258 (1963). URL <https://link.aps.org/doi/10.1103/PhysRev.129.2252>.
- [61] Chien, W. S. & Brown, R. E. Study of the $\alpha + \alpha$ system below 15 MeV (c.m.). *Phys. Rev. C* **10**, 1767–1784 (1974). URL <https://link.aps.org/doi/10.1103/PhysRevC.10.1767>.
- [62] Chamon, L. C., Carlson, B. V. & Gasques, L. R. $\alpha + \alpha$ scattering reexamined in the context of the são paulo potential. *Phys. Rev. C* **83**, 034617 (2011). URL <https://link.aps.org/doi/10.1103/PhysRevC.83.034617>.
- [63] Bredin, D. J. *et al.* The scattering of alpha particles by helium. *Proceedings of the Royal Society of London. Series A, Mathematical and Physical Sciences* **251**, 143–155 (1959). URL <http://www.jstor.org/stable/100757>.
- [64] Darriulat, P. *Contribution à l'étude de l'interaction $\alpha - \alpha$* . Ph.D. thesis, University of Paris (1965).
- [65] Darriulat, P., Igo, G., Pugh, H. G. & Holmgren, H. D. Elastic scattering of alpha particles by helium between 53 and 120 MeV. *Phys. Rev.* **137**, B315–B325 (1965). URL <https://link.aps.org/doi/10.1103/PhysRev.137.B315>.
- [66] Gutbrod, H., Winn, W. & Blann, M. Measurement and interpretation of heavy ion fusion excitation functions. *Nuclear Physics A* **213**, 267–284 (1973).

- [67] Gavron, A. Statistical model calculations in heavy ion reactions. *Phys. Rev. C* **21**, 230–236 (1980). URL <https://link.aps.org/doi/10.1103/PhysRevC.21.230>.
- [68] Tarasov, O. & Bazin, D. Lise++: Radioactive beam production with in-flight separators. *Nuclear Instruments and Methods in Physics Research Section B: Beam Interactions with Materials and Atoms* **266**, 4657–4664 (2008).

Acknowledgments. We warmly acknowledge Prof. H. Lenske, Prof. N. Barnea, Prof. W. Leidemann and the late Prof. A. Vitturi for enlightening discussions. We warmly acknowledge Prof. E. Hiyama, Prof. U.-G Meißner and Dr. S. Shen for providing us with their density distributions. We warmly acknowledge the technical staff of INFN-LNS for the support. We also warmly acknowledge M. D’ Andrea for the technical support with the OSCAR set-up. The project has received funding from the European Research Council (ERC) under the European Union’s Horizon 2020 research and innovation programme (grant agreement No. 714625). S.B. acknowledges support by the Deutsche Forschungsgemeinschaft (DFG) through the Cluster of Excellence “Precision Physics, Fundamental Interactions, and Structure of Matter” PRISMA⁺ EXC 2118/1 (Project ID 39083149) and through CRC1660: Hadrons and Nuclei as discovery tools (Project No. 514321794). L.C. acknowledges financial support by Fundação de Amparo à Pesquisa do Estado de São Paulo (FAPESP) Proc. No 2019/07767-1, Conselho Nacional de Desenvolvimento Científico e Tecnológico (CNPq) Proc. No 302072/2022-5, and project INCT-FNA Proc. No 464898/2014-5.

Author Contributions. F.C., S.B., D.C., M.Cav., C.A., G.O and L.C. proposed the experiment. F.C., V.S., D.C., M.Cav. and I.L. performed the experimental set-up with a contribution from H.-W.B., S.C., C.C., M.Cin., O.S., A.S. and M.Vig.. F.C., V.S., D.C., M.Cav., I.L., C.A., G.A.B., S.C., M.Cic., I.C., C.F., A.H., M.H., Y.K., O.S., A.S., D.T. and A.Y. performed the data taking. V.S. performed the data reduction with a contribution from F.C., D.C., M.Cav., M.F., M.Cic., M.Cin., D.D., A.H., T.M. and O.S.. V.S. and F.C. performed the line shape analysis. L.C. performed coupled-channel cross section calculations with a contribution from F.C., V.S. and Y.K.. S.B., G.O., M.Viv., A.K. collected or/and calculated densities from ab-initio calculations. F.C., V.S., S.B., L.C., G.O. and M.Viv. wrote the manuscript. All the authors have revised the manuscript.

Competing interests. The authors declare no competing interests.

Supplementary Information. Supplementary Information accompanies this paper.

Supplementary Information

Probing nuclear interactions à la Rutherford: Insights on ^4He from α scattering

Contents

1	Supplementary Methods	2
1.1	Reaction Theory Details	2
1.1.1	Adopted potentials in the reaction theory	4
1.2	Ab-initio theory details	5
1.2.1	Nuclear densities: bound-state vs continuum approach	6
2	Supplementary Figures	9
3	Supplementary Tables	15
	Supplementary References	16

1 Supplementary Methods

1.1 Reaction Theory Details

We have performed cross section calculations for the α - α elastic and inelastic scattering in the framework of the coupled channel quantum scattering theory [1]. A set of two coupled equations is written for each component l of the angular momentum of the relative motion of one α with respect to other α as

$$\begin{aligned} \left[-\frac{\hbar^2}{2\mu} \frac{d^2}{dR^2} + \frac{l(l+1)}{2\mu R^2} + U_1(R) \right] \psi_l^{(1)} + U_{\text{coup}}(R) \psi_l^{(2)} &= E_{\text{cm}} \psi_l^{(1)}, \\ \left[-\frac{\hbar^2}{2\mu} \frac{d^2}{dR^2} + \frac{l(l+1)}{2\mu R^2} + U_2(R) \right] \psi_l^{(2)} + U_{\text{coup}}(R) \psi_l^{(1)} &= (E_{\text{cm}} - E_X) \psi_l^{(2)}, \end{aligned} \quad (1)$$

where the wavefunctions for the elastic and inelastic channels have the following asymptotic behavior:

$$\begin{aligned} \psi_l^{(1)}(R \rightarrow \infty) &= \frac{i}{2} \left[H_l^- - S_l^{(1)} H_l^+ \right], \\ \psi_l^{(2)}(R \rightarrow \infty) &= -\frac{i}{2} S_l^{(2)} H_l^+, \end{aligned} \quad (2)$$

and H_l^\pm represent the Coulomb Hankel functions for the respective channel. Since we deal with identical particles of spin zero, we must consider only even values of l . U_1 is the diagonal nucleus-nucleus optical potentials in the initial state interaction (ISI), which is the same as the final state interaction (FSI) only in the case of the elastic scattering process. For the inelastic channel, the U_2 optical potential represents the FSI, while U_{coup} is the coupling potential.

We assume the following model for the diagonal part of the ISI and FSI interactions in Eq. (1)

$$U_j(R) = V_j^{(C)}(R) + N_{Rj} V_j^{(N)}(R) + i N_{Ij} V_j^{(N)}(R), \quad j = 1, 2 \quad (3)$$

where $V^{(C)}$ and $V^{(N)}$ are the Coulomb and nuclear potentials. N_{Rj} and N_{Ij} are normalization factors for the real and imaginary parts of the optical potential for the elastic channel ($j = 1$) that we use in our analyses. The corresponding values are dependent on the angular momentum l , as explained below. For the inelastic channel, we set $N_{R2} = 1$ and $N_{I2} = 0$.

We obtain the Coulomb and nuclear potentials for the diagonal parts of the interaction within the double folding model, namely through

$$V_j(\vec{R}) = \int \rho_{0_1^+}(\vec{r}_1) \rho_{0_j^+}(\vec{r}_2) v_{NN}(\vec{R} - \vec{r}_1 + \vec{r}_2) d\vec{r}_1 d\vec{r}_2, \quad (4)$$

where $\rho_{0_1^+}(\vec{r}_1)$ is the ${}^4\text{He}$ density in its ground-state 0_1^+ . Here, $\rho_{0_j^+}(\vec{r}_2)$ is the density of either the 0_1^+ or the 0_2^+ when dealing with $U_1(R)$ and $U_2(R)$, respectively. For

the coupling potential, U_{coup} , we adopt a similar double-folding procedure as that of Eq. (4), where the second density is this time replaced by the transition density $\rho_{0_1^+ \rightarrow 0_2^+}$.

In Eq. 4, v_{NN} represents the effective nuclear plus Coulomb interactions. For such a force, we use the Brazilian Nuclear potential (BNP) [2, 3] to calculate the nuclear part of the double-folding potentials. Although the nucleon-nucleon force used in the folding is different from the Hamiltonian used in the ab-initio densities, this ‘‘inconsistency’’ is absorbed in the modeling intrinsic to the double-folding approach. Within this model, we adopt matter densities ($\rho = \rho_m$) in equation (4), which is related to the distribution of nucleons ρ_N as [2]

$$\rho_m(r) = \int \rho_N(|\vec{r} - \vec{r}'|) \rho_{m/N}(r') d\vec{r}', \quad (5)$$

where $\rho_{m/N}$ is associated to the intrinsic matter density of one nucleon (which is equal the intrinsic charge density of one proton). Since the nucleon is not a point-like particle and has a finite size, the matter density of the nucleus $\rho_m(r)$ is different—through Eq. (5)—from the point-like distribution of nucleons in the nucleus $\rho_N(r)$ [2, 3].

For the case of ${}^4\text{He}$, where the number of protons is equal to the number of neutrons, we assume that the matter density is twice the charge density, for both the 0_1^+ and 0_2^+ states, and adopt the experimental charge density obtained from electron scattering experiments of Ref. [4] to describe the ground state. It is important to note that the use of g.s. densities from ab-initio for the 0_1^+ state instead of that from the experimental charge does not significantly modify the diagonal double-folding potentials for either channel.

The calculation of the folding potential is performed through Fourier transform method [5–7]), which for the coupling potential reads

$$U_{\text{coup}}(R) = \frac{1}{2\pi^2} \int \hat{v}_{NN}(q) \hat{\rho}_{0_1^+}(q) \hat{\rho}^{0_1^+ \rightarrow 0_2^+}(q) J_0(qR) q^2 dq, \quad (6)$$

where $J_0(x) = \sin(x)/x$ is the spherical Bessel function of order zero, $\hat{\rho}_{0_1^+}$ is the Fourier transform of the (matter or charge) 0_1^+ density,

$$\hat{\rho}_{0_1^+}(q) = 4\pi \int \rho_{0_1^+}(r) J_0(qr) r^2 dr, \quad (7)$$

and \hat{v}_{NN} is the Fourier transform of the nucleon-nucleon and Coulomb interactions. The term $\hat{\rho}^{0_1^+ \rightarrow 0_2^+}$ in Eq. (6) is the Fourier transform of the matter transition density

$$\hat{\rho}_0^{g.s. \rightarrow 0_2^+}(q) = \sqrt{4\pi} \int \rho_0^{g.s. \rightarrow 0_2^+}(r) J_0(qr) r^2 dr. \quad (8)$$

As done for the diagonal densities, we assume the matter transition density to be twice the charge transition density. This ansatz is used in Eq. (6) to obtain the nuclear and Coulomb coupling potentials, respectively. In similar form as in Eq. (5),

the transition density of charge (or matter) is related to the respective distribution of protons (or nucleons) by

$$\rho_{\text{charge or matter}}^{0_1^+ \rightarrow 0_2^+}(r) = \int \rho_{\text{protons or nucleons}}^{0_1^+ \rightarrow 0_2^+}(|\vec{r} - \vec{r}'|) \rho_{m/N}(r') d\vec{r}', \quad (9)$$

Equation (9) results in the following correlation among the respective transforms

$$\hat{\rho}_{\text{charge or matter}}^{0_1^+ \rightarrow 0_2^+}(q) = \hat{\rho}_{\text{protons or nucleons}}^{0_1^+ \rightarrow 0_2^+}(q) \times \hat{\rho}_{m/N}(q), \quad (10)$$

where the Fourier transform for the proton finite size factor is well known from electron scattering experiments

$$\hat{\rho}_{m/N}(q) \approx \frac{1}{(1 + 0.0552 q^2)^2}. \quad (11)$$

In Supplementary Figs. 3(a-c) we present the diagonal and transition matter densities obtained from the corresponding nucleon densities reported on Refs. [8–11].

1.1.1 Adopted potentials in the reaction theory

At low energies ($E_{\text{Lab}} < 34.6$ MeV), the only open reaction channel for ${}^4\text{He} + {}^4\text{He}$ is the capture process with γ decay, ${}^4\text{He}({}^4\text{He}, \gamma){}^8\text{Be}$, followed by the break-up of the beryllium into two α -particles. However, this process has a very small cross section. Thus, in this energy region, we can neglect the absorption of flux from the elastic channel. In this condition, the optical potential for the elastic channel must have vanishing imaginary part ($N_{I1} = 0$). In addition, all the respective elements of the S matrix must have unitary modulus. Therefore, each of these elements is characterized just by the respective phase-shift. Furthermore, considering that only a small number of waves contribute to the scattering, in this low-energy region the elastic scattering angular distribution depends on a small number of even partial waves (typically $l = 0, 2, 4$ and 6). Due to the small number of free parameters, the phase-shifts were obtained quite accurately as a function of the energy from elastic scattering data analyses.

In Supplementary Fig. 4, we show the $l = 0, 2, 4, 6$ phase-shifts and moduli of the S matrix (for the elastic channel), as a function of the energy. The experimental values in the figure were obtained in several works [12–21] and we emphasize (through pink star symbols) the data from Ref. [21] at $E_{\text{Lab}} = 53.4$ MeV and 63.9 MeV. Indeed, these energies are close to the energies of the inelastic scattering data analyzed in the present work: 53.0 MeV and 63.8 MeV. The red solid lines in Supplementary Fig. 4 represent the results obtained with the standard BNP adopting $N_{R1} = 1$ and $N_{I1} = 0$ in Eq. (3). It is clear that the standard BNP provides a quite good description of the experimental phase-shifts in the low energy region.

For energies above the threshold mentioned above, $E_{\text{Lab}} > 34.6$ MeV, the experimental phase-shifts deviate from the BNP predictions (see Supplementary Fig. 4), probably due to effects of the polarization arising from the couplings to all the open reaction channels. In addition, at these energies the modulus of S is not unitary anymore, as can be clearly observed from the experimental values presented in the

figures. These deviations can be effectively taken into account in the theoretical calculations through the renormalization of the nuclear potential, adjusting the N_{R1} and N_{I1} parameters in the $U_1(R)$ potential.

We have tuned the values of N_{R1} and N_{I1} for the elastic channel in order to reproduce, as well as possible, the phase-shifts and the modulus of S at the energies of $E_{\text{Lab}} = 53.4$ MeV and $E_{\text{Lab}} = 63.9$ MeV (pink star symbols in Supplementary Fig. 4). The adjustment was performed separately for each l value. The corresponding best N_{R1} and N_{I1} values are provided in Supplementary Table 2. The respective theoretical results for phase-shifts and moduli of S are indicated by the blue dashed lines in Supplementary Fig. 4, which show a reasonable agreement with the experimental values in the region $50 \leq E_{\text{Lab}} \leq 65$ MeV. Note, in Supplementary Table 2, that the N_{R1} values are only slightly different from 1, except in the case of $l = 6$. Observe also that the N_{I1} values are small, about $N_{I1} = 0.1$. This indicates a small but non negligible overall polarization and absorption effect induced by the reaction channels not explicitly included in our coupled channel equations.

1.2 Ab-initio theory details

Theoretical approaches in which nuclear properties are derived from virtually exact solutions of the Schrödinger equation for nucleons interacting via two- and three-body forces—commonly known as ab initio methods—have been extensively tested on light nuclei. Besides the famous benchmark [22] for the α -particle ground-state, ab-initio theory has been recently challenged by the transition form factor $F_M(0_1^+ \rightarrow 0_2^+)$ of the α -particle. We describe the various calculations below in chronological order, as they constitute the motivation for the present work.

The first calculation, performed in 2004 by Hiyama et al. [8], achieved a good agreement with experimental electron scattering data for F_M , despite employing a relatively simple Hamiltonian. A subsequent study by Bacca et al. [23] in 2013, using realistic chiral effective field theory (χ EFT) potentials, significantly overestimated the experimental values. This discrepancy raised questions about either the accuracy of realistic Hamiltonians or the reliability of the experimental data. The latter possibility was recently ruled out by a high-precision measurement by Kegel et al. [24], which confirmed the earlier experimental results with much improved accuracy. As a result, the tension with the realistic theory has intensified, prompting a wave of new theoretical calculations—some of which are consistent with the experimental data [10, 11, 25], while others continue to show disagreement [26].

Michel et al. [25], in a calculation that neglected three-body forces managed to reproduce the Kegel data by tuning the Hamiltonian to fit the 0_2^+ resonance position to experiment, $E_r \approx 0.4$ MeV [27]. However, a mistake was subsequently found [28], leading to the real energy of the Gamow pole to be 0.12 MeV. Meißner et al. [11] obtained the correct description of the Kegel et al. data in the framework of nuclear lattice EFT adopting a simple Hamiltonian, which is based on the SU(4) isospin symmetry. The parameter of this Hamiltonian were calibrated on a variety of data including medium-mass nuclei, excluding the position of the 0_2^+ resonance, which nevertheless is

correctly reproduced. However, the Fourier transform of the obtained transition density in coordinate space (see Fig. 2 of Ref. [11]) is about 20% higher than the form factor presented in Fig. 1 of the same reference.

These facts expose the unexpected situation in which possibly realistic Hamiltonians did not reproduce the monopole transition strength, while simpler Hamiltonians did. However, another calculation by Viviani et al. [10] reproduced F_M with realistic chiral EFT Hamiltonians—though different from those used in Ref. [23]— but found a low E_T . Moreover, Yin et al. [26] performed a calculation with no-core shell model using the Daejeon16 potential, a different realistic Hamiltonian, obtaining a result very similar to [23], therefore not consistent with experimental data. Finally, the 0_2^+ state has been subject of a recent benchmark study using sophisticated techniques to solve the four-body problem, namely the solution of the Faddeev-Yakuboski, the Alt-Grassberger-Sandhas equations and the hyperspherical harmonics method [29]. Without considering the Coulomb interaction this state results bound and very close to the p - ^3H threshold. In this case the 0_1^+ and 0_2^+ can be identified as the two Efimov four-body states attached to the lowest three-body Efimov state, in this case the triton [30]. Including the Coulomb interaction the 0_2^+ state crosses the p - ^3H threshold and moves into the continuum becoming a resonance [29].

Given the puzzling situation, we have to find other ways to probe the 0_2^+ state in the α -particle. Ab-initio calculations can deliver a density for 0_1^+ and 0_2^+ , as well as a transition density from 0_1^+ to 0_2^+ . They can be used as input in reaction theory to construct potentials within the double folding model, and then be compared with experimental data. In this work, we collect densities from the following calculations: Hiyama et al. [8], Meißner et al. [11], Bacca et al. [9, 23], and Viviani et al. [10]. The first two calculations use simple Hamiltonians, while the second two use realistic chiral EFT interactions with the same two-body force [31, 32] at next-to-next-to-next-to-leading order (N3LO) with cutoff $\Lambda = 500$, and a three-body force derived at next-to-next-to-leading order (N2LO) [33]. The latter contains two free parameters, namely the coupling constant multiplying the one-pion-exchange (c_D) and that multiplying the contact term (c_E). These two parameters are different in Ref. [9] and [10]: c_D and c_E are fixed to reproduce ^3H and ^4He binding energies following [34] in [9], while they are fit to reproduce the ^3H binding energy and the Gamow-Teller matrix element of tritium beta decay [35] in [10]. Both calculations [23] and [10] are performed using the hyperspherical harmonics (HH) expansion method [10, 36–40], where one can construct either bound states or continuum states, as explained below.

1.2.1 Nuclear densities: bound-state vs continuum approach

From the point of view of ab-initio calculations, the nuclear densities used in Sect. 1.1 are defined as

$$\rho_{a,b}(r) = \langle \Psi_a | \sum_{j=1}^4 \delta(\mathbf{r}_j - \mathbf{r}) | \Psi_b \rangle, \quad (12)$$

where $a, b = 0_1^+, 0_2^+$ and $\Psi_{0_1^+}$ ($\Psi_{0_2^+}$) is the ^4He ground state (first excited state) wave function.

For the ground state, the wave function can be obtained from an expansion over a complete set of orthonormal square-integrable basis states Φ_ν as

$$\Psi_{0_1^+} = \sum_{\nu=1}^N a_\nu \Phi_\nu . \quad (13)$$

The Hamiltonian represented on this basis $M_{\nu,\nu'} = \langle \Phi_\nu | H | \Phi_{\nu'} \rangle$ is then used in the eigenvalue problem $\sum_{\nu'} M_{\nu,\nu'} a_{\nu'} = E_\nu a_\nu$, which is solved for increasing N . The lowest eigenvalue is the ${}^4\text{He}$ ground state energy $E_{0_1^+}$. When hyperspherical harmonics are used as the basis, this variational approach is called the HH method [10, 39, 40]. To speed up the convergence in N , but renouncing to the variational property, an effective interaction can be introduced leading to a method called EHH [37, 38]. For infinite N , both the HH and EHH approaches converge to the same exact result, provided that the same Hamiltonian is used.

Regarding $\Psi_{0_2^+}$, we have two choices. First, in a bound-state approximation, we can select the second lowest eigenvalue of the above eigenvalue problem to be $E_{0_2^+}$ and construct $\Psi_{0_2^+}$ with the associated coefficients a_ν .

The corresponding densities in Eq. (12) are normalizable, since $\Psi_{0_2^+}$ is written in terms of square integrable states.

However, this state is not a true bound state but a resonance, rapidly decaying in a proton and a ${}^3\text{H}$ nucleus. Therefore the second option is to calculate $\Psi_{0_2^+}$ in the continuum. Using the HH formulation of Refs. [10, 39, 40] we have computed the $p + {}^3\text{H}$ scattering wave functions Ψ_E , where E is now the (positive) kinetic energy of the two clusters p and ${}^3\text{H}$ when they are well apart. The total energy of this scattering state (with respect to the ground state, and therefore corresponding to the energy transferred to the α -target) is $E_T = E + E_{th}$, where E_{th} is the threshold energy given by the difference between the ${}^4\text{He}$ and ${}^3\text{H}$ binding energies. We can also introduce the relative inter-cluster momentum q_{ic} , defined to be $q_{ic}^2/2\mu = E$, where μ is the $p + {}^3\text{H}$ reduced mass. The wave function Ψ_E can be calculated using the HH method (see Ref. [10]) as well, but this time in the expansion we have to include also non-square-integrable functions, describing the motion of the $p + {}^3\text{H}$ when they are far from each other. Explicitly,

$$\Psi_E = \sum_{\nu=1}^N a_\nu \Phi_\nu + \Psi_A , \quad (14)$$

where Ψ_A is the asymptotic non-square-integrable part. The first term of Eq. (14) is non zero only where the four nucleons are close to each other. When the $p + {}^3\text{H}$ distance is above 20 fm, Ψ_E reduces to Ψ_A .

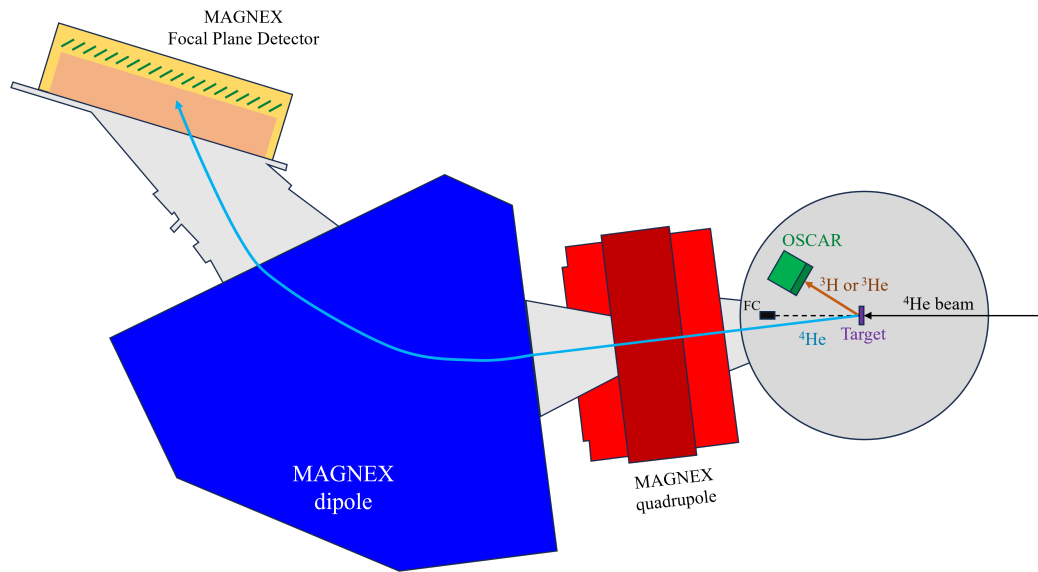
In the range of energies probed in our experiment, the S-wave $p + {}^3\text{H}$ phase shift $\delta(E)$ has a typical resonance behavior, namely a sharp increase reaching the value of 90° . In such a case, Ψ_E tends to have the form of a ‘‘quasi-bound’’ state, namely to be very large in the region where the four nucleons are close to each other, much larger than Ψ_A . In a time-dependent formalism, this means that the four particles tend to stay for a long time together before the system falls apart as a $p + {}^3\text{H}$ scattering state.

The short-range behavior of Ψ_E is very similar to $\Psi_{0_2^+}$, calculated as a bound state. To show this, we have calculated the following densities

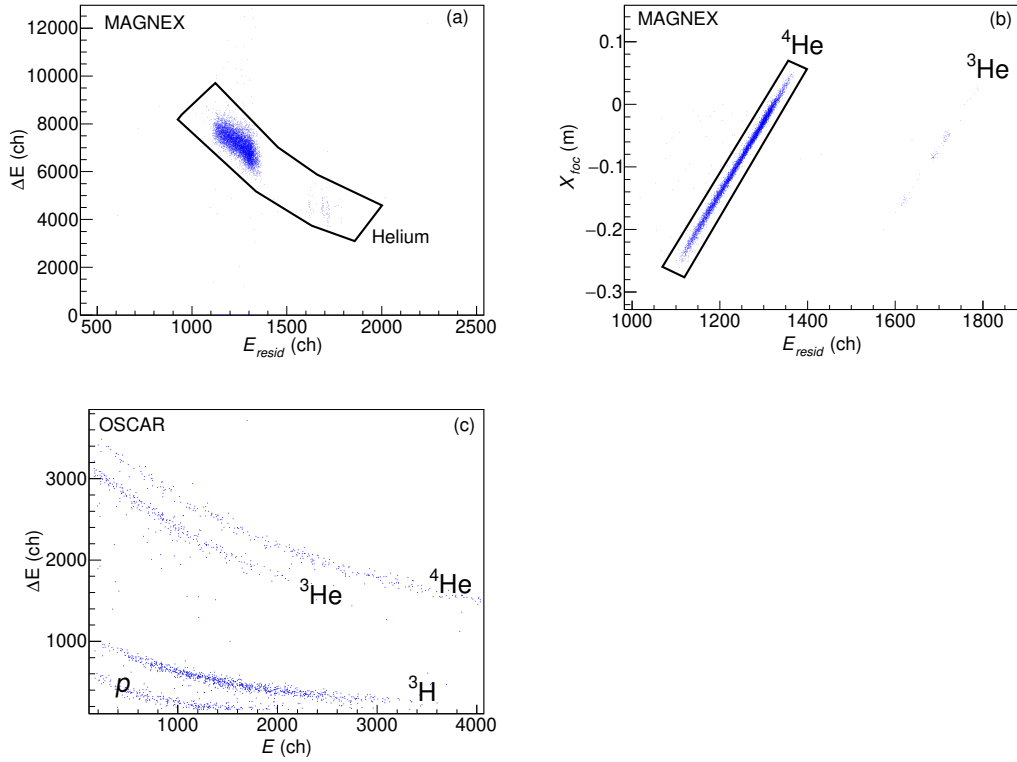
$$\rho_{0_1^+,E}(r) = \langle \Psi_{0_1^+} | \sum_{j=1}^4 \delta(\mathbf{r}_j - \mathbf{r}) | \Psi_E \rangle, \quad \rho_E(r) = \langle \Psi_E | \sum_{j=1}^4 \delta(\mathbf{r}_j - \mathbf{r}) | \Psi_E \rangle. \quad (15)$$

The density $\rho_E(r)$ (see Supplementary Fig. 7 for its distribution as a function of r for different E) cannot be normalized, since $\int d^3r \rho_E(r) = \infty$. In fact, for large r it goes like $\rho_E(r) \rightarrow \sin^2(q_{ic}r + \delta)/r^2$. In particular, as $E \rightarrow 0.20$ MeV, the particle density for $r < 1$ fm rapidly increases, showing the formation of a quasi-bound state. In Supplementary Fig. 3(d) we compare the calculated $\rho_{0_2^+,0_2^+}(r)$ with $\alpha \times \rho_E(r)$, rescaled so that $\alpha \times \rho_E(r=0) = \rho_{0_2^+,0_2^+}(0)$. Since in our experiment, we mainly probe $p + {}^3\text{H}$ energies in the region $0.35 < E < 0.65$ MeV, we have reported in the figure $\rho_{E=0.35 \text{ MeV}}$, $\rho_{E=0.50 \text{ MeV}}$, and $\rho_{E=0.65 \text{ MeV}}$. As it can be seen by inspecting the figure, the various densities are quite similar. The $\rho_E(r)$ curves are large when $r < 1$ fm and have the same plateau as $\rho_{0_2^+,0_2^+}$, and then they decrease in a similar way. Only for large r , there would be large differences (not visible in the figure), as $\rho_{0_2^+,0_2^+}$ goes rapidly to zero, while ρ_E has the oscillating behavior mentioned above. We can observe the same similarities in $\rho_{0_1^+,0_2^+}$ and $\rho_{0_1^+,E}$. As a consequence, we can safely apply the bound-state densities to study the ${}^4\text{He} + {}^4\text{He}$ reaction.

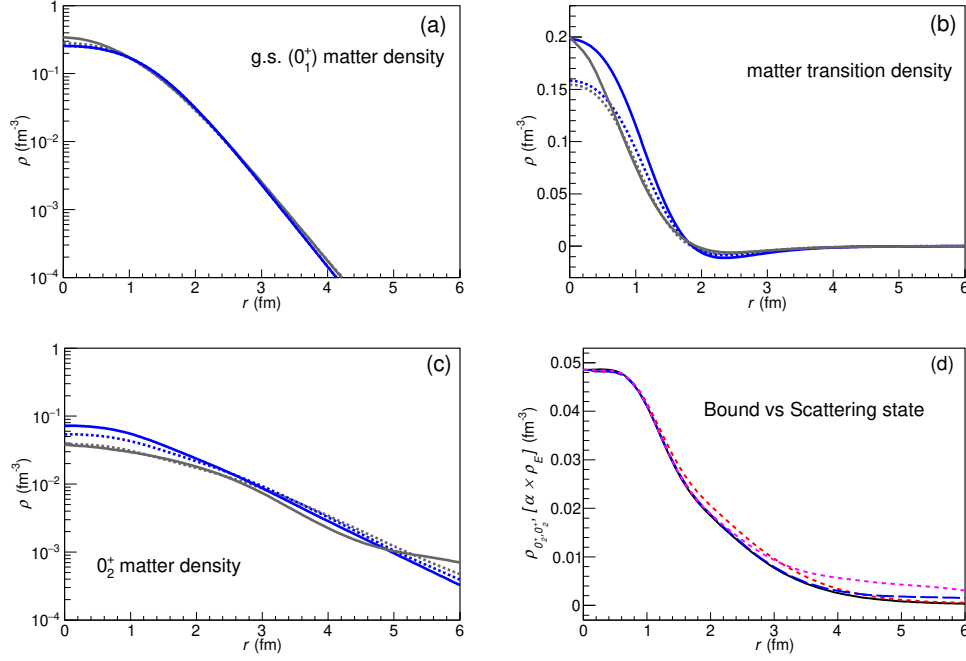
2 Supplementary Figures



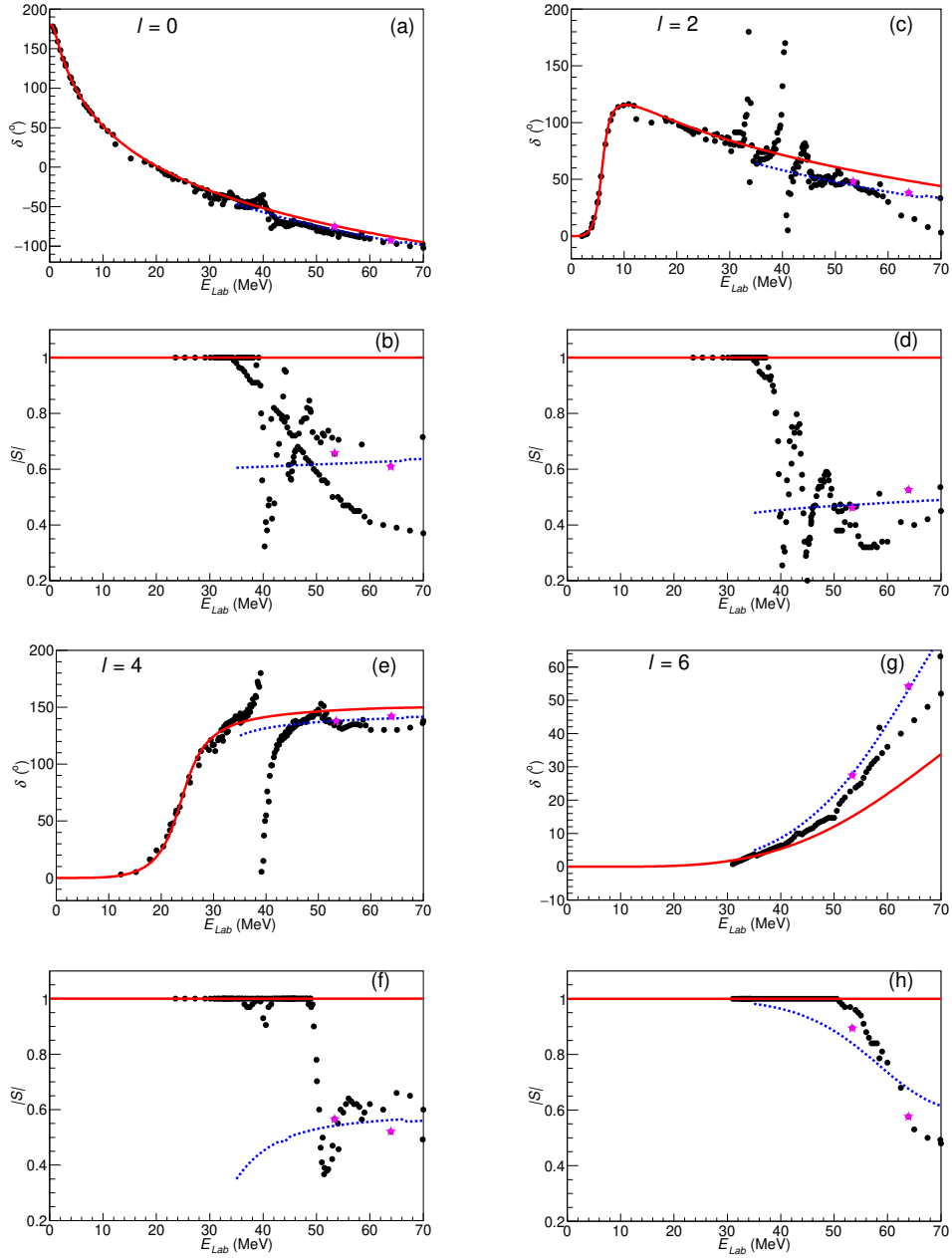
Supplementary Fig. 1 Experimental set-up. Illustration of the experimental set-up for the exclusive measurement (the scattering chamber is not in scale for a better readability). The cyan blue arrow represents a symbolic sketch of the trajectory of a ^4He ejectile across the MAGNEX spectrometer while the orange arrow the trajectory of ^3H or ^3He decay products detected in coincidence by the OSCAR telescope.



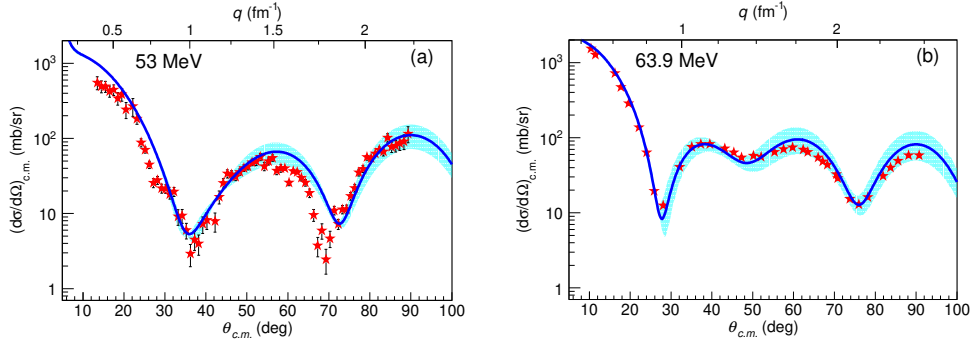
Supplementary Fig. 2 Particle identification spectra. (a) A typical ΔE versus residual energy (E_{resid}) spectrum for a single silicon detector of MAGNEX Focal Plane Detector (FPD). (b) Horizontal position (X_{foc}) versus residual energy (E_{resid}) spectrum for a single silicon detector of the MAGNEX FPD after applying the graphical selection of $Z=2$ (Helium) of the panel (a). (c) A typical ΔE versus residual energy (E) spectrum for a combination of a single ΔE strip correlated with a single E pad of OSCAR.



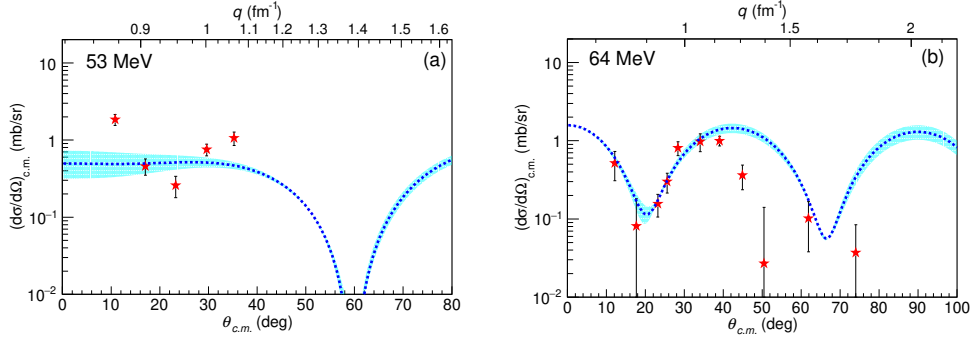
Supplementary Fig. 3 Calculated densities. (a) Matter density (ρ) for the ${}^4\text{He}$ g.s. derived (see section 1.1) from Refs. [9] (Bacca et al. - χEFT), [10] (Viviani et al. - χEFT), [11] (Meißner et al.) and [8] (Hiyama et al.) are depicted with the blue solid, blue dashed, grey solid and grey dashed lines, respectively. (b) Same as in (a) but, for the transition matter densities. (c) Same as in (a) but, for the 0_2^+ state. (d) Calculated density $\rho_{0_2^+, 0_2^+}(r)$ denoted with the black solid line is compared with the $[\alpha \times \rho_E(r)]$, rescaled so that $\alpha \times \rho_E(r=0) = \rho_{0_2^+, 0_2^+}(0)$. Calculations for $E = 0.35$ MeV, $E = 0.50$ MeV and $E = 0.65$ MeV are denoted with the red, blue and magenta dashed lines, respectively. See Methods - Calculation methodology and Supplementary Methods (1.2.1) for details.



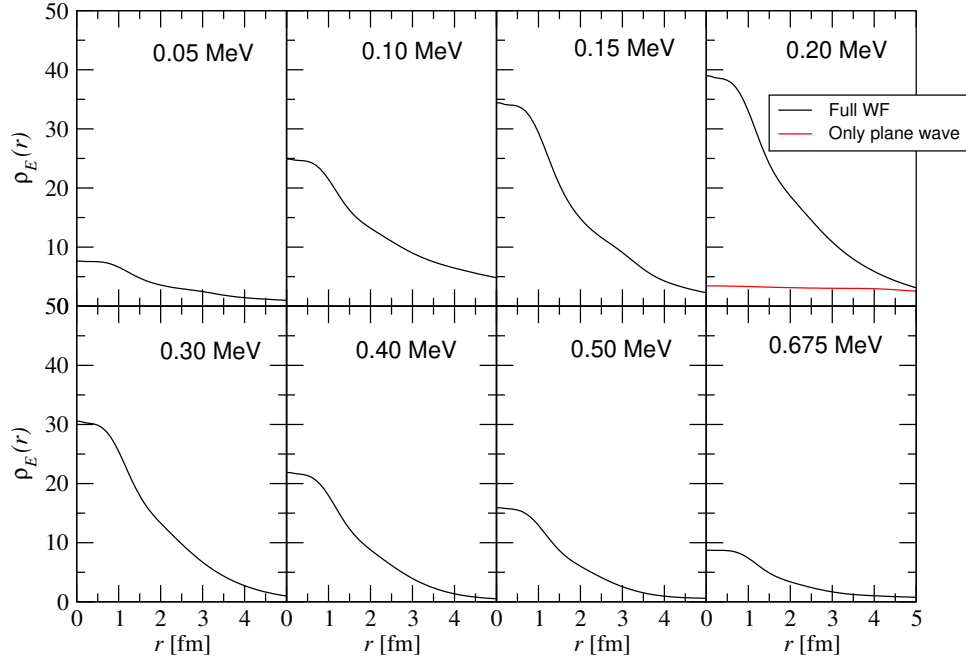
Supplementary Fig. 4 Phase-shift (δ) and modulus of the S matrix. Experimental values [12–21] for the phase-shift δ (a, c, e, g) and modulus of the S matrix (b, d, f, h), obtained for the elastic channel, as a function of the energy for $l = 0$, $l = 2$, $l = 4$ and $l = 6$, respectively. The data of Ref. [21] at 53.4 and 63.9 MeV, similar incident energies with the present analysis, are emphasized with the magenta stars. The red solid lines in the figure represent the predictions of the standard Brazilian Nuclear Potential (BNP). The blue dashed lines were obtained considering the renormalization of the BNP through the N_R and N_I values discussed in Supplementary Methods (1.1.1).



Supplementary Fig. 5 Elastic scattering angular distributions and uncertainties in the reaction modeling. (a) Experimental elastic scattering angular distribution at 53 MeV (red stars) compared with theoretical calculations taking into account a phase shift analysis using the data of Ref. [21] at 53.4 and 63.9 MeV (blue solid line). The error bars correspond to the combination of uncertainties coming from the solid angle and detection efficiency estimation, the uncertainties in the beam current and the target thickness determination, the statistical error and the background subtraction. (b) Same but for the incident energy of 63.9 MeV with experimental data from Ref. [21]. In both panels, the cyan blue band accounts for the uncertainties in the reaction modeling.



Supplementary Fig. 6 Inelastic scattering angular distributions and uncertainties in the reaction modeling. Experimental data (red stars) for the 0_2^+ resonance at 53 MeV (a) and 64 MeV [41] (b) incident beam energy are compared with the theoretical reaction cross sections using the chiral effective field theory densities from Ref. [10], denoted with the blue dashed line (presented also in Fig. 3 of the main article). The error bars in panel (a) correspond to the combination of uncertainties coming from the solid angle and detection efficiency estimation, the uncertainties in the beam current and the target thickness determination, the statistical error and the background subtraction. The error bars in panel (b) were taken from Ref. [41]. The cyan blue band accounts for the uncertainties in the reaction modeling, common to all calculations but shown here only for the effective field theory densities of Ref. [10].



Supplementary Fig. 7 $\rho_E(r)$ density as defined in Eq. (15), without applying any rescaling factor. The black and red solid lines represent results adopting the full and the plane wave-functions, respectively (see Supplementary Methods 1.2.1). As $E \rightarrow 0.20$ MeV, the particle density for $r < 1$ fm rapidly increases, showing the formation of a quasi-bound state. For the present example the parameters of the resonance can be extracted from $\delta(E)$, and are those given in Refs [29, 42].

3 Supplementary Tables

Supplementary Table 1 Total reaction and inelastic scattering cross sections. The total reaction cross section deduced from the imaginary part of the ISI ($\sigma_{\text{tot}}^{\text{th}}$) is compared with that extracted from our experimental data and fusion reaction calculations ($\sigma_{\text{tot}}^{\text{exp}}$). An estimation of the experimental and theoretical inelastic scattering cross section is also denoted as $\sigma_{\text{inel}}^{\text{exp}}$ and $\sigma_{\text{inel}}^{\text{th}}$, respectively.

	cross section	angular range
$\sigma_{\text{tot}}^{\text{exp}}$	370 ± 70 mb	Full
$\sigma_{\text{tot}}^{\text{th}}$	370 ± 90 mb	Full
$\sigma_{\text{inel}}^{\text{exp}}$	1.35 ± 0.25 mb	$7.7^\circ \leq \theta_{\text{c.m.}} \leq 38.4^\circ$
$\sigma_{\text{inel}}^{\text{th}}$	1.64 ± 0.28 mb	$7.7^\circ \leq \theta_{\text{c.m.}} \leq 38.4^\circ$
$\sigma_{\text{inel}}^{\text{th}}$	9.5 ± 1.6 mb	Full

Supplementary Table 2 N_{R1} and N_{I1} values. N_{R1} and N_{I1} as a function of l from the fit of the experimental S matrix (elastic scattering) for $E_{\text{Lab}} = 53.4$ MeV and $E_{\text{Lab}} = 63.9$ MeV.

l	N_{R1}	N_{I1}
0	0.974	0.066
2	0.933	0.105
4	0.948	0.091
6	1.384	0.096

Supplementary References

- [1] Satchler, G. R. *Direct Nuclear Reactions* (Oxford University Press, Oxford, 1983).
- [2] Chamon, L., Carlson, B. & Gasques, L. São Paulo potential version 2 (SPP2) and Brazilian nuclear potential (BNP). *Computer Physics Communications* **267**, 108061 (2021). URL <https://www.sciencedirect.com/science/article/pii/S0010465521001739>.
- [3] Chamon, L. C., Gasques, L. R. & Carlson, B. V. Approximate treatment of relativistic effects in the low-energy $\alpha + \alpha$ scattering. *Phys. Rev. C* **84**, 044607 (2011). URL <https://link.aps.org/doi/10.1103/PhysRevC.84.044607>.
- [4] De Vries, H., De Jager, C. & De Vries, C. Nuclear charge-density-distribution parameters from elastic electron scattering. *Atomic Data and Nuclear Data Tables* **36**, 495–536 (1987). URL <https://www.sciencedirect.com/science/article/pii/0092640X87900131>.
- [5] Satchler, G. & Love, W. Folding model potentials from realistic interactions for heavy-ion scattering. *Physics Reports* **55**, 183–254 (1979). URL <https://www.sciencedirect.com/science/article/pii/0370157379900814>.
- [6] Takigawa, N., Rumin, T. & Ihara, N. Coulomb interaction between spherical and deformed nuclei. *Phys. Rev. C* **61**, 044607 (2000). URL <https://link.aps.org/doi/10.1103/PhysRevC.61.044607>.
- [7] Chamon, L. C. & Morales-Botero, D. F. Folding-type coupling potentials in the context of the generalized rotation–vibration model. *Journal of Physics G: Nuclear and Particle Physics* **45**, 035104 (2018). URL <https://doi.org/10.1088/1361-6471/aaa8b5>.
- [8] Hiyama, E., Gibson, B. F. & Kamimura, M. Four-body calculation of the first excited state of ${}^4\text{He}$ using a realistic nn interaction: ${}^4\text{He}(e, e'){}^4\text{He}(0_2^+)$ and the monopole sum rule. *Phys. Rev. C* **70**, 031001 (2004). URL <https://link.aps.org/doi/10.1103/PhysRevC.70.031001>.
- [9] Bacca, S., Barnea, N., Leidemann, W. & Orlandini, G. Examination of the first excited state of ${}^4\text{He}$ as a potential breathing mode. *Phys. Rev. C* **91**, 024303 (2015). URL <https://link.aps.org/doi/10.1103/PhysRevC.91.024303>.
- [10] Viviani, M., Kievsky, A., Marcucci, L. E. & Girlanda, L. Study of the alpha-particle monopole transition form factor. *Few Body Systems* **65**, 74 (2024). URL <https://doi.org/10.1007/s00601-024-01940-2>.
- [11] Meißner, U.-G., Shen, S., Elhatisari, S. & Lee, D. Ab initio calculation of the alpha-particle monopole transition form factor. *Phys. Rev. Lett.* **132**, 062501 (2024). URL <https://link.aps.org/doi/10.1103/PhysRevLett.132.062501>.

- [12] Russell, J. L., Phillips, G. C. & Reich, C. W. Scattering of alpha particles from helium. *Phys. Rev.* **104**, 135–142 (1956). URL <https://link.aps.org/doi/10.1103/PhysRev.104.135>.
- [13] Heydenburg, N. P. & Temmer, G. M. Alpha-alpha scattering at low energies. *Phys. Rev.* **104**, 123–134 (1956). URL <https://link.aps.org/doi/10.1103/PhysRev.104.123>.
- [14] Nilson, R., Kerman, R. O., Briggs, G. R. & Jentschke, W. Alpha-alpha particle scattering in the energy range 12.3 to 22.9 MeV. *Phys. Rev.* **104**, 1673–1680 (1956). URL <https://link.aps.org/doi/10.1103/PhysRev.104.1673>.
- [15] Bacher, A. D. *et al.* Observation of high-lying levels in ^8Be from $\alpha - \alpha$ elastic scattering. *Phys. Rev. Lett.* **29**, 1331–1333 (1972). URL <https://link.aps.org/doi/10.1103/PhysRevLett.29.1331>.
- [16] Tombrello, T. A. & Senhouse, L. S. Elastic scattering of alpha particles from helium. *Phys. Rev.* **129**, 2252–2258 (1963). URL <https://link.aps.org/doi/10.1103/PhysRev.129.2252>.
- [17] Chien, W. S. & Brown, R. E. Study of the $\alpha + \alpha$ system below 15 MeV (c.m.). *Phys. Rev. C* **10**, 1767–1784 (1974). URL <https://link.aps.org/doi/10.1103/PhysRevC.10.1767>.
- [18] Chamon, L. C., Carlson, B. V. & Gasques, L. R. $\alpha + \alpha$ scattering reexamined in the context of the são paulo potential. *Phys. Rev. C* **83**, 034617 (2011). URL <https://link.aps.org/doi/10.1103/PhysRevC.83.034617>.
- [19] Bredin, D. J. *et al.* The scattering of alpha particles by helium. *Proceedings of the Royal Society of London. Series A, Mathematical and Physical Sciences* **251**, 143–155 (1959). URL <http://www.jstor.org/stable/100757>.
- [20] Darriulat, P. *Contribution à l'étude de l'interaction $\alpha - \alpha$* . Ph.D. thesis, University of Paris (1965).
- [21] Darriulat, P., Igo, G., Pugh, H. G. & Holmgren, H. D. Elastic scattering of alpha particles by helium between 53 and 120 MeV. *Phys. Rev.* **137**, B315–B325 (1965). URL <https://link.aps.org/doi/10.1103/PhysRev.137.B315>.
- [22] Kamada, H. *et al.* Benchmark test calculation of a four-nucleon bound state. *Phys. Rev. C* **64**, 044001 (2001).
- [23] Bacca, S., Barnea, N., Leidemann, W. & Orlandini, G. Isoscalar monopole resonance of the alpha particle: A prism to nuclear hamiltonians. *Phys. Rev. Lett.* **110**, 042503 (2013). URL <https://link.aps.org/doi/10.1103/PhysRevLett.110.042503>.

- [24] Kegel, S. *et al.* Measurement of the α -particle monopole transition form factor challenges theory: A low-energy puzzle for nuclear forces? *Phys. Rev. Lett.* **130**, 152502 (2023). URL <https://link.aps.org/doi/10.1103/PhysRevLett.130.152502>.
- [25] Michel, N., Nazarewicz, W. & Płoszajczak, M. Description of the proton-decaying 0_2^+ resonance of the α particle. *Phys. Rev. Lett.* **131**, 242502 (2023). URL <https://link.aps.org/doi/10.1103/PhysRevLett.131.242502>.
- [26] Yin, P. *et al.* α -particle monopole form factors within the ab initio no-core shell model. *Phys. Rev. C* **112**, L031303 (2025). URL <https://link.aps.org/doi/10.1103/1pxs-xjtl>.
- [27] Tilley, D., Weller, H. & Hale, G. Energy levels of light nuclei $A = 4$. *Nuclear Physics A* **541**, 1–104 (1992).
- [28] Michel, N., Nazarewicz, W. & Płoszajczak, M. Erratum: Description of the proton-decaying 0_2^+ resonance of the α particle [phys. rev. lett. 131, 242502 (2023)]. *Phys. Rev. Lett.* **133**, 239901 (2024). URL <https://link.aps.org/doi/10.1103/PhysRevLett.133.239901>.
- [29] Duerinck, P.-Y. *et al.* Excited state of the α particle: A benchmark study. *Phys. Rev. C* **112**, 044001 (2025). URL <https://link.aps.org/doi/10.1103/jcd4-8jh8>.
- [30] Platter, L., Hammer, H.-W. & Meißner, U.-G. Four-boson system with short-range interactions. *Phys. Rev. A* **70**, 052101 (2004). URL <https://link.aps.org/doi/10.1103/PhysRevA.70.052101>.
- [31] Entem, D. R. & Machleidt, R. Accurate charge-dependent nucleon-nucleon potential at fourth order of chiral perturbation theory. *Phys. Rev. C* **68**, 041001 (2003). URL <https://link.aps.org/doi/10.1103/PhysRevC.68.041001>.
- [32] Machleidt, R. & Entem, D. R. Chiral effective field theory and nuclear forces. *Phys. Rept.* **503**, 1–75 (2011).
- [33] Epelbaum, E. *et al.* Three nucleon forces from chiral effective field theory. *Phys. Rev. C* **66**, 064001 (2002).
- [34] Navrátil, P. Local three-nucleon interaction from chiral effective field theory. *Few-Body Systems* **41**, 117 (2007). URL <https://doi.org/10.1007/s00601-007-0193-3>.
- [35] Baroni, A. *et al.* Local chiral interactions, the tritium Gamow-Teller matrix element, and the three-nucleon contact term. *Phys. Rev. C* **98**, 044003 (2018).
- [36] Efros, V. D. Application of the hyperspherical basis in the theory of few-nucleon systems. *Soviet Journal of Nuclear Physics* **29**, 526 (1979). Originally published in *Yadernaya Fizika* 29, 1055 (1979).

- [37] Barnea, N., Leidemann, W. & Orlandini, G. State dependent effective interaction for the hyperspherical formalism. *Phys. Rev. C* **61**, 054001 (2000). URL <https://link.aps.org/doi/10.1103/PhysRevC.61.054001>.
- [38] Barnea, N., Leidemann, W. & Orlandini, G. State-dependent effective interaction for the hyperspherical formalism with noncentral forces. *Nuclear Physics A* **693**, 565 – 578 (2001). URL <http://www.sciencedirect.com/science/article/pii/S0375947401007941>.
- [39] Kievsky, A., Rosati, S., Viviani, M., Marcucci, L. & Girlanda, L. A High-precision variational approach to three- and four-nucleon bound and zero-energy scattering states. *J. Phys. G* **35**, 063101 (2008).
- [40] Marcucci, L. E. *et al.* The hyperspherical harmonics method: A tool for testing and improving nuclear interaction models. *Frontiers in Physics* **8** (2020). URL <https://www.frontiersin.org/journals/physics/articles/10.3389/fphy.2020.00069>.
- [41] Gross, E. E., Hungerford, E. V., Malanify, J. J., Pugh, H. G. & Watson, J. W. Investigation of the reaction ${}^4\text{He}({}^4\text{He}, {}^4\text{He}){}^4\text{He}^*$ at 64 MeV. *Phys. Rev.* **178**, 1584–1590 (1969). URL <https://link.aps.org/doi/10.1103/PhysRev.178.1584>.
- [42] Viviani, M., Girlanda, L., Kievsky, A. & Marcucci, L. E. $n + {}^3\text{H}$, $p + {}^3\text{He}$, $p + {}^3\text{H}$, and $n + {}^3\text{He}$ scattering with the hyperspherical harmonic method. *Phys. Rev. C* **102**, 034007 (2020). URL <https://link.aps.org/doi/10.1103/PhysRevC.102.034007>.